UNIVERSITY OF CALIFORNIA

Santa Barbara

# Analysis of Electromigration in Nanofluidics

A dissertation submitted in partial satisfaction of the

requirements for the degree Doctor of Philosophy

in Mechanical Engineering

by

Yu-Wei Liu

Committee in charge:

Professor Carl D. Meinhart, Chair

Professor Sumita Pennathur

Professor Kimberly Turner

Professor Luke Theogarajan

June 2015

The dissertation of Yu-Wei Liu is approved.

_____

Sumita Pennathur

_____

Kimberly Turner

_____

Luke Theogarajan

_____

Carl D. Meinhart, Committee Chair

June 2015

Analysis of Electromigration in Nanofluidics



by

Yu-Wei Liu

# ACKNOWLEDGEMENTS

This work would not have been possible without help and support of many people. I would like to express my deepest gratitude to my advisor, Professor Carl Meinhart for his support, patience, and guidance. He showed me how to approach a problem effectively and provided me with a good atmosphere for doing research. I am grateful to Professor Sumita Pennathur for providing me the great opportunity to work on the nanoparticle electrophoresis project. Her insights inspire me to see the problem in a different way. I would like to thank my committee members Professor Kimberly Turner and Professor Luke Theogarajan for offering valuable suggestions to improve this work.

It is my pleasure to work with members of Meinhart Lab. Their help in this work is highly appreciated. I would like to take this opportunity to express my gratitude to them: Marin Sigurdson, Brian Piorek, Nimisha Srivastava, Meysam R. Barmi, Chrysafis Andreou, Mehran R. Hoonejani, Nicholas Judy, and Eric Terry. I want to thank Tom Wynne for helpful discussions about experiments and simulations. I would also like to thank Professor Noel MacDonald, Changsong Ding, Payam Bozorgi, TJ Reed in TGP project.

I would like to thank my friends for their help and support: Min-Chi, Ming-Feng, Yi-Tai, Martin, Yeh-Shin, Ming-Yen, Chung-Jen, and Chien-Cheng. Finally, I want to express my greatest thankfulness to my parents, my brother Yuchuan for their unconditional love and support.

VITA OF YU-WEI LIU

June 2015

## EDUCATION

Ph.D., Mechanical Engineering, University of California Santa Barbara, June 2015

Master of Science, Mechanical Engineering, National Taiwan University, Taiwan, June 2006

Bachelor of Science, Mechanical Engineering, National Taiwan University, Taiwan, June 2004

## EXPERIENCE

Application Engineer
COMSOL Inc., Los Angeles, July 2012 - September 2012

Graduate Student Researcher,
Department of Mechanical Engineering, University of California Santa Barbara, 2010 - 2015

Teaching Assistant,
Department of Mechanical Engineering, University of California Santa Barbara, 2009 - 2012

## PUBLICATIONS

**Y. Liu**, S. Pennathur, C. D. Meinhart, "Electro migration of 2D Nanorods in Nanochannels," (submitted)

**Y. Liu**, S. Pennathur, C. D. Meinhart, "Electrophoretic Mobility of a Spherical Nanoparticle in a Nanochannel," *Physics of Fluids*, 26.11 (2014) 112002.

M. Sigurdson, **Y. Liu**, P. Bozorgi, D. Bothman, N. MacDonald, C. D. Meinhart, "A Large Scale Titanium Thermal Ground Plane," *International Journal of Heat and Mass Transfer*, 62 (2013), 178-183.

## CONFERENCE PROCEEDINGS

**Y. Liu**, S. Pennathur, C. D. Meinhart, "Electrophoretic Mobility of Nanoparticles Confined in Nanochannels," 2014 AIChE Annual Meeting (2014).

**Y. Liu**, T. Wynne, S. Pennathur, C. D. Meinhart, "Electrophoretic Mobility of Spherical Nanoparticles Confined in Nanochannels," 66th Annual Meeting, APS DFD (2013).

**Y. Liu**, M. Sigurdson, C. D. Meinhart, "Capillary Driven Flow through Optimal Wick Structures," 65th Annual Meeting, APS DFD (2012).

**Y. Liu**, M. Sigurdson, P. Bozorgi, N. MacDonald, C. D. Meinhart, "Optimum Transport in Flat Heat Pipes," 64th Annual Meeting, APS DFD (2011).

**PATENT**

P. Bozorgi, C. D. Meinhart, M. Sigurdson, N. MacDonald, D. Bothman, **Y. Liu**, "Titanium-Based Thermal Ground Plane", U.S. Patent 20130327504, issued Dec. 12, 2013.

ABSTRACT

Analysis of Electromigration in Nanofluidics

by

Yu-Wei Liu

Numerical simulation is used to calculate the electrophoretic mobility of a charged spherical nanoparticle confined in a nanochannel, under a weakly applied electric field. Classic models for electrophoretic mobility are valid only in the linear regime of small particle zeta potential, and for an unbounded fluid domain. However, these models fail to predict the electrophoretic mobility measured experimentally in bounded nanochannels. We adopt asymptotically-expanded formulations and solve the fully-coupled equations on a 3D finite element domain. Factors affecting particle mobility include electrolyte concentration, channel size, and zeta potentials on both the particle surface and channel walls. Specifically, spherical particles are examined with diameters $2a$ = 10 and 50 nm, in a 100 nm high channel. The non-dimensional electric double layers were varied between $0.1 < \kappa a < 100$. The results indicate that the mobility of a particle located at the nanochannel centerline agrees to within 1% of the average mobility of a particle distributed transversely throughout the nanochannel. Furthermore, confinement by the nanochannel walls was found to affect greatly nanoparticle mobility. As a result, it is feasible to use nanochannels to separate two different size nanoparticles, even when the particles have equal zeta potentials. Finally, a

new method is proposed to estimate accurately particle and wall zeta potentials by contrasting the observed differences in mobility in two different height channels.

Next, two-dimensional nanorods are simulated numerically to study the electromigration within nanoscale fluidic channels. We improved on an existing steady-state model to include fluid-structure interaction and capture dynamics of moving nanorods. Specifically, we investigate the motion of a 2 nm × 3.4 nm two-dimensional rod-like particle (representative of 10 bp DNA) in a 100 nm two-dimensional channel under an applied external electric field. The results show that due to the interaction between the electric double layers (EDLs) of the particle and the channel walls, the particle is confined to the centerline of a channel with thick EDLs. In contrast, an oscillatory motion is observed for thin EDLs, which can be explained by examining the electrophoretic and hydrodynamic forces and moments on the particle. Although thermal fluctuations are not modeled, and could negate the effects of the oscillatory motion in practical systems, the effect is still of value to understand. We calculate the electrophoretic mobility of these confined nanorods and compare the results with the approximated mobility from our steady-state model. Although the thick EDL systems match well, the results show an up to 10% difference in mobility of the two models for the 50 mM electrolyte concentration, which indicates that the fluid-structure interaction is important for mobility of non-spherical particles, in thin double-layer systems.

Finally, we use our model to estimate particle zeta potential by measured mobility from several experiments. The results show that our model is required to capture double layer polarization and double layer interaction. In addition, the composition of electrolyte solution is important in determining the particle mobility as well as the zeta potential.

TABLE OF CONTENTS

# 1. Introduction

## *1.1. Background and Motivation*

Electrokinetic phenomena in microchannels and nanochannels contribute to many practical applications in colloidal and biomedical sciences [1-3]. For example, the electrophoretic mobility of a charged particle can be used to characterize its zeta potential [4], which is the key parameter for determining the stability of colloid dispersions. In addition, the separation of different colloidal and analyte species in a microfluidic device can be applied to directly identify biomolecules and particles for a variety of different applications, for example, disease diagnosis [5, 6]. A particle behaves differently in a channel compared to an unbounded domain, especially when the thickness of electric double layer (EDL) is on the order of channel size. The confinement effect not only induces additional hydrodynamic drag on the particle, but also affects the electric field near the particle, thereby altering the resulting electrophoretic force. Therefore, a comprehensive model is required to capture the underlying coupled physics.

Electrokinetic phenomena in EDL have been studied extensively [7-18], including specifically the electrophoretic mobility of particles [19-28]. Smoluchowksi [22] and Huckel [23] studied limiting cases of thin and thick EDLs on both particles and surfaces, and obtained a simple linear relation between electrophoretic mobility and particle zeta potential. Henry [24] derived an expression for electrophoretic mobility of a spherical particle with a finite EDL thickness. However, these studies only focused on the linear regime, i.e. using small zeta potentials. Wiersema et al. [25] calculated mobility of a particle for high zeta

potentials using a Gouy-Chapman model for the EDL. O'Brien and White [26] later directly solved the linearized equations for a particle of high zeta potentials from low to high electrolyte concentration. They found that the linear relation between mobility and zeta potential is only valid for low zeta potential cases. As the zeta potential increases, the electrophoretic mobility reaches a maximum and then decreases in a thin double layer system. This is because the drag force increases faster with increasing zeta potential than the driving electric force. Ohshima et al. [27] derived an analytical expression for the mobility of a spherical particle in a symmetric electrolyte solution. This expression agrees well with the results of O'Brien and White. Khair and Squires [28] showed the slip enhances particle mobility for thick double layers by reducing viscous drag. In the case of thin double layers, however, mobility increases from low to moderate values (0 to 50 mV) of zeta potential. Further increases in zeta potential leads to decreased mobility, and approach a limiting value independent of slip length, due to nonuniform surface conduction.

In terms of examining the mobility of particles in confined systems, the boundary effects for spheres located near walls have been widely studied [29-34]. Keh and Anderson [29] studied a non-conducting sphere near a boundary for a very thin EDL on the particle. A charged boundary generates electro-osmotic flow, which affects both electrical and velocity fields. Keh and Chen [30] derived an analytical expression of electrophoretic mobility of a charged spherical particle near a charged plane wall in the thin EDL limit. When the gap between the particle and the wall is small, the mobility is enhanced up to 23%, due the squeezed electrical field lines. Ennis and Anderson [31] used method of reflections to study a spherical particle near a charged wall and in a cylindrical pore. Later Shugai and Carnie [32] studied similar problems with different methods. They found that the linear relation

between electrophoretic mobility and zeta potential does not hold due to complex EDL interactions. Hsu et al. [33] analyzed electrophoretic mobility of a spherical particle in a confined cylindrical pore with linearized equations assuming a low particle zeta potential. In the case of both charged particle and pore, they found that the magnitude of mobility has a local maximum as electrolyte concentration increases, which is due to the interaction of the double layer between the particle and the pore. Hsu and Chen [34] then extended their model to include the effects of double layer polarization and electro-osmotic flow caused by the charged pore. For a positively charged particle in a positively charged pore with low surface potential, the mobility has a minimum and the direction of the motion may change twice as double layer thickness changes. To summarize, in all cases to date, electrophoresis of a particle is only considered under certain restrictions (low zeta potential, very thin or thick EDL) in an unbounded or idealized domain (spherical/cylindrical pore). However, these studies can never accurately capture nanochannel experimental data, where the zeta potential is not low, the EDL is of variable thickness (not limited to thick or thin) and the domain is a fixed rectangular system.

In addition, the geometry of particles may not be perfect spheres in practical cases. Electrophoresis of nanoparticles with different shapes in confined channels is important for many applications such as particle separation and particle manipulation [35-36], and has been widely studied both experimentally [37-40] and theoretically [31-34, 41-45]. Nanoparticle mobility is affected by a variety of variables, most importantly zeta potential, electrolyte concentration, channel geometry and the inherent nanoparticle geometry. Importantly, for cases when the thickness of EDL is on the order of the channel size, the interaction of particles and the channel walls alters both the hydrodynamic drag and the

electrophoretic force on the particles [45]. Although there have been many models of particles in channels with thin EDL approximations [31,32,42], it is important to have a model that can include all couple physics required to describe the complicated particle dynamics, since in many realistic systems, the EDL is not thin [38-40].

Typically, a steady-state assumption is used to formulate electrophoretic models of spherical particles. However, the electrophoretic-driven motion of non-spherical particles is inherently unsteady. Non-spherical particles can translate and rotate during electrophoretic motion, and the hydrodynamic drag depends upon particle geometry and the orientation relative to the flow. Davison and Sharp [46] investigated the transient motion of 2D rod-like particles in a narrow channel, although, as mentioned above, they assumed thin EDLs. They studied different initial particle orientations and observed an oscillatory motion without thermal fluctuations. Furthermore, they found that the particle mobility increases when the particle is near the walls due to the increased electric field. Ai and Qian [47] investigated the electrokinetic translocation of a 2D rod-like particle through a nanopore. However, in this case, the EDL of the particle was assumed not to be affected by the external electric field or the EDL of the solid boundary. In addition, previous models did not investigate the initial orientation of the particle, which can affect both translational velocity and rotation. EDLs can align nanorods, which must be accounted for in a numerical model.

Therefore, we use numerical simulation to investigate the mobility of spherical particles in channels under steady-state assumption. Then we improve our steady-state model to include fluid-structure interaction to track motion of a non-spherical particle. Finally we use our model to estimate particle zeta potential by the measured mobility from experiments.

### *1.2. Outline*

In chapter 2, we introduce the electrokinetic equations and derive the linearized equations by using asymptotic expansion. We assume the flow is incompressible and Reynolds number and Péclet number are small due to the small length scale of the system. The ionic potential is introduced to simplify Nernst-Planck equations.

In chapter 3, numerical simulation is used to examine the mobility of a charged spherical particle of any size EDL driven by a weak electric field in a rectangular channel, where the magnitude of the applied electric field is much smaller than the electric field generated inside the EDL. We solve the fully-coupled equations on a 3D domain. The results are first validated in an unbounded domain with existing theory. Next, the effect of particle location in the nanochannel is examined. The results indicate that the mobility of a particle distributed transversely throughout the nanochannel agrees to within 1% of a particle located at the nanochannel centerline. Using the centerline for particle location, we investigated particle mobilities for varying zeta potentials and electrolyte concentrations, which showed a large dependence on EDL thickness and channel height. We next investigate the ability to improve separation efficacy of particles in a nanochannel. Finally, a new method is proposed to characterize accurately particle and wall zeta potentials, by comparing observed particle mobilities measured in microchannels to those measured in nanochannels.

In chapter 4, we improve upon our steady-state model [45] to include fluid-structure interactions, in order to investigate the mobility and the confinement effect of a charged 2D nanorod driven by an applied electric field in a nanochannel. We adopt the formulations

from our previous work for electric potential, flow motion, and electrolyte concentration, and add solid mechanics for the particle displacement. The results show that the EDL thickness has significant influence on the particle motion within the nanochannel. Confined movement of a particle is observed for low electrolyte concentration, and the oscillatory behavior for high electrolyte concentration can be explained by examining the force and moment on the particle. Although these effects may be small compared to thermal fluctuations, it is still insightful to understand and explain these innate deterministic behaviors. Finally, we study the particle distribution histograms to understand how the distribution of particles within the channel affects particle mobility, and compare these results with our steady-state model. The results indicate that the estimated mobility from the steady-state model is accurate for 1 mM electrolyte concentration, but overpredicts by 10% for the 50 mM case. Therefore, the current time-dependent fluid-structure simulation model is required for the accurate mobility of non-spherical particles in thin double-layer systems.

In chapter 5 we apply our model to estimate particle zeta potential. It shows that the effects of electromigration and thermal fluctuations are insignificant for 3D spherical particles with diameter greater than 50 nm. Therefore we can use the steady-state model and the measured particle mobility to estimate particle zeta potential. The results show that the classic models (Smoluchowksi [22], Huckel [23]) cannot be used to calculate particle zeta potential because they exclude the effects of double layer polarization and double layer interaction. In addition, finite particle zeta potential cannot be obtained for some cases because the measured mobility is greater than the maximum value predicted by the model. Since buffer solutions were used in experiments, the complexity of the electrolyte could affect the particle mobility. The particle mobility in different electrolyte solution is also

calculated to show the effect of the composition of electrolyte. Finally we will give some conclusions and future directions in chapter 6.

## 2. Theory of Electrokinetics

When a charged surface is in contact with an electrolyte solution, conterions would be attracted near the surface to form electric double layer. If an external electric field is applied, the electric force on the ions will induce fluid motion such as electro-osmosis and electrophoresis. In this chapter we introduce the equations used to describe electrokinetic motion.

### *2.1. Governing Equations*

Consider a particle in a channel filled with electrolyte with $z_i$ valence of ions under an external applied electric field. The electric potential follows Poisson equation:

$$\nabla^2\phi = -\frac{\rho}{\varepsilon}, \tag{2.1}$$

where $\phi$ is electric potential, $\rho = e\sum z_i n_i$ is charge density, $\varepsilon$ is permittivity, e is electron charge, and $n_i$ are ion number concentration of species *i*. The flow motion is described by Navier-Stokes equations, which can be reduced to Stokes equations under the assumptions of incompressible flow and small Reynolds number. In addition, the Coulomb body force term should be included due to the charged fluid:

$$\nabla \cdot \mathbf{u} = 0 \tag{2.2}$$

$$\eta\nabla^2\mathbf{u} - \nabla p - \rho\nabla\phi = 0, \tag{2.3}$$

where $\mathbf{u}$ is flow velocity, *p* is pressure, $\eta$ is fluid viscosity. Nernst-Planck equations are used to describe the distribution of ion concentrations:

$$\nabla \cdot \left[ D_i \left( \nabla n_i + \frac{ez_i}{k_B T} n_i \nabla \phi \right) - n_i \mathbf{u} \right] = 0, \tag{2.4}$$

where $D_i$, $k_B$, $T$, are the diffusion coefficient of species $i$, Boltzmann constant, temperature, respectively. Note that the temporal term is neglected due to small Péclet number. In the next section we use proper characteristic length, concentration and potential to scale the governing equations.

### *2.2. Dimensionless Equations*

Here we use $\phi_c = k_B T / e$, the particle radius $a$, the ionic strength $I = \frac{1}{2} \sum n_{i\infty} z_i^2$ to scale electric potential, length, ion number concentration, respectively. Note that the ionic strength $I$ can be reduced to the bulk concentration $n_\infty$ if the electrolyte is monovalent and symmetric, that is, $n_\infty = n_{1\infty} = n_{2\infty}$ and $z_1 = -z_2 = 1$. Then the velocity scale from electrophoretic velocity is $U_c = \varepsilon \phi_c E_\infty / \eta$, where $E_\infty$ is the external electric field. The pressure scale is $p_c = \eta U_c / a$, and the electric and hydrodynamic force scales are $F_{c,ele} = \rho_c a^3 (\phi_c / a) = I k_B T a^2$ and $F_{c,hyd} = \eta U_c a$. In addition, we define ion Péclet number $\alpha_i = 2 U_c a / D_i$ and Debye length as $\lambda_D = \frac{1}{\kappa} = \sqrt{\frac{\varepsilon k_B T}{2 e^2 I}}$. As a result we have the dimensionless equations as follows:

$$\nabla^2 \hat{\phi} = -\frac{1}{2} (\kappa a)^2 \hat{\rho} \tag{2.5}$$

$$\nabla \cdot \left[ \nabla \hat{n}_i + z_i \hat{n}_i \nabla \hat{\phi} - \frac{1}{2} \alpha_i \hat{n}_i \hat{\mathbf{u}} \right] = 0 \tag{2.6}$$

$$\nabla \cdot \hat{\mathbf{u}} = 0 \tag{2.7}$$

$$\nabla^2\hat{\mathbf{u}} - \nabla\hat{p} - \beta\hat{\rho}\nabla\hat{\phi} = 0, \tag{2.8}$$

where $\beta = F_{c,ele} / F_{c,\,flow}$ represents the ratio of electric force scale to hydrodynamic force scale.

### *2.3. Asymptotic Expansion*

Following the work of Khair and Squires [28], if the applied electric field is weak, a regular perturbation expansion can be used to simplify the governing equations. Suppose particle zeta potential is a constant value $\zeta_p$, the scale of electric field in the electric double layer (EDL) is $\zeta_p / \lambda_D$. Next, a small parameter $\delta$ is defined as the ratio of applied electric field to the electrostatic field, that results from surface charge on the nanoparticle, $\delta \equiv E_\infty / \zeta_p \kappa$, where $E_\infty$ is the applied electric field. The order of $\delta$ is about $O\left(10^{-2}\right)$ in most cases. The dependent variables are expanded as follows:

$$\hat{\phi} = \hat{\phi}_0 + \delta\hat{\phi}_1 + O\left(\delta^2\right) \tag{2.9}$$

$$\hat{n}_i = \hat{n}_{i0} + \delta\hat{n}_{i1} + O\left(\delta^2\right) \tag{2.10}$$

$$\hat{\mathbf{u}} = \hat{\mathbf{u}}_0 + \delta\hat{\mathbf{u}}_1 + O\left(\delta^2\right) \tag{2.11}$$

$$\hat{p} = \hat{p}_0 + \delta\hat{p}_1 + O\left(\delta^2\right). \tag{2.12}$$

Here, the subscript "0" corresponds to electrostatic condition (no applied electric field), while subscript "1" corresponds to perturbed state. After substituting Equations (2.9)-(2.12) into Equations (2.5)-(2.8), we obtain zeroth and first order equations as following.

### *2.4. Electrostatic State*

After collecting zeroth order terms we have the following equations:

$$\nabla^2 \hat{\phi}_0 = -\frac{1}{2}(\kappa a)^2 \hat{\rho}_0 \tag{2.13}$$

$$\nabla \cdot \left[ \nabla \hat{n}_{i0} + z_i \hat{n}_{i0} \nabla \hat{\phi}_0 - \frac{1}{2} \alpha_i \hat{n}_{i0} \hat{\mathbf{u}}_0 \right] = 0 \tag{2.14}$$

$$\nabla \cdot \hat{\mathbf{u}}_0 = 0 \tag{2.15}$$

$$\nabla^2 \hat{\mathbf{u}}_0 - \nabla \hat{p}_0 - \beta \hat{\rho}_0 \nabla \hat{\phi}_0 = 0 \,. \tag{2.16}$$

The zeroth order equations describe the electrostatic state, that is, a particle sitting in a static fluid domain. Since the velocity field $\mathbf{u}_0$ should be zero, from Nernst-Planck equation (2.14) we find that the concentration should obey Boltzmann distribution

$$\hat{n}_{i0} = \exp\left(- z_i \hat{\phi}_0\right). \tag{2.17}$$

Substituting the above equation into Poisson equation we obtain Poisson-Boltzmann equation

$$\nabla^2 \hat{\phi}_0 = -\frac{1}{2}(\kappa a)^2 \sum z_i \exp\left(- z_i \hat{\phi}_0\right). \tag{2.18}$$

The above equation can be solved numerically with proper boundary conditions. In addition, from Stokes equation (2.16) we find that the hydrostatic pressure field still exists without flow motion

$$- \nabla \hat{p}_0 - \beta \hat{\rho}_0 \nabla \hat{\phi}_0 = 0 \,. \tag{2.19}$$

Note that this hydrostatic pressure results in zero net force on the particle.

### *2.5. Weakly Applied Electric Field*

The first order equations correspond to perturbation of the system under a weak applied electric field:

$$\nabla^2\hat{\phi}_1 = -\frac{1}{2}(\kappa a)^2\hat{\rho}_1 \tag{2.20}$$

$$\nabla\cdot\left[\nabla\hat{n}_{i1} + z_i\left(\hat{n}_{i0}\nabla\hat{\phi}_1 + \hat{n}_{i1}\nabla\hat{\phi}_0\right) - \frac{1}{2}\alpha_i\hat{n}_{i0}\hat{\mathbf{u}}_1\right] = 0 \tag{2.21}$$

$$\nabla\cdot\hat{\mathbf{u}}_1 = 0 \tag{2.22}$$

$$\nabla^2\hat{\mathbf{u}}_1 - \nabla\hat{p}_1 - \beta\left(\hat{\rho}_0\nabla\hat{\phi}_1 + \hat{\rho}_1\nabla\hat{\phi}_0\right) = 0. \tag{2.23}$$

Since Nernst-Planck equations are highly coupled (involving $\hat{n}_{i1}$, $\hat{\phi}_1$, $\hat{\mathbf{u}}_1$), we can rewrite the equations by defining ionic potential $\hat{\Theta}_1 = -\frac{\hat{n}_{i1}}{z_i\hat{n}_{i0}} - \hat{\phi}_1$:

$$\nabla^2\hat{\Theta}_i - z_i\nabla\hat{\phi}_0\cdot\nabla\hat{\Theta}_i - \frac{1}{2}\alpha_i\hat{\mathbf{u}}_1\cdot\nabla\hat{\phi}_0 = 0. \tag{2.24}$$

The above equations are greatly simplified compared with the original equations. The ion concentration can be obtained by $\hat{n}_{i1} = z_i\hat{n}_{i0}\left(-\hat{\Theta}_1 - \hat{\phi}_1\right)$ after ionic potentials are obtained. Proper boundary conditions for both electrostatic and perturbed states are required to solve the complete system. In next chapters we solve the above system of equations to study electrophoresis of spherical and rod-like particles in two- or three-dimensional domains.

# 3. Spherical Nanoparticles in Nanochannels

In this chapter we solve the electrokinetic equations to investigate mobility of spherical nanoparticles in nanochannels. The steady-state assumption is adopted and the forces on the particle are calculated to obtain the particle velocity. Finally we will show possible applications of nanochannels in separation of particles and measurement of zeta potential. The work in this chapter is reproduced with permission from [Electrophoretic Mobility of a Spherical Nanoparticle in a Nanochannel, Phys. Fluids 26, 112002 (2014)]. Copyright [2014], AIP Publishing LLC. (http://dx.doi.org/10.1063/1.4901330)

## *3.1. Equations and Numerical Simulation*

### 3.1.1. Governing Equations

Consider a spherical particle in a channel filled with electrolyte with valences of $z_1$ and $z_2$ of cations and anions respectively as shown in Figure 3.1. The flow is assumed to be incompressible due to assumed low Reynolds number flow in nanoconfined channels. To simplify the system, we further assume that the electrolyte is symmetric and monovalent (KCl for example), that is, $z_1 = -z_2 = 1$. Thus the bulk ion concentrations and diffusion coefficients are simplified as $n_{1\infty} = n_{2\infty} = n_\infty$, $D_1 = D_2 = D$. Following the work of chapter 2, for a weakly applied electric field, a regular perturbation expansion can be used to simplify the governing equations. Suppose particle zeta potential is a constant value $\zeta_p$, the scale of electric field in the EDL is $\zeta_p / \lambda_D$, where $\lambda_D = 1/\kappa = \left(\varepsilon k_B T / 2 n_\infty e^2\right)^{1/2}$ is Debye length. Next, a small parameter $\delta$ is defined as the ratio of applied electric field to the electrostatic field,

resulting from the surface charge on the nanoparticle, or $\delta \equiv E_\infty \lambda_D / \zeta_p$, where $E_\infty$ is the applied electric field. Here we assume the following constants: $E_\infty \sim 1000\text{V/m}$, $\lambda_D \sim 10^{-8}\,\text{m}$, $\zeta_p \sim 10^{-2}\,\text{V}$, so $\delta$ is $O\left(10^{-3}\right)$.

The dimensionless governing equations can then be rewritten as electrostatic and perturbed equations as follows:

$$\nabla^2 \hat{\phi}_0 = (\kappa a)^2 \sinh \hat{\phi}_0, \tag{3.1}$$

$$\nabla^2 \hat{\phi}_1 = -\frac{1}{2}(\kappa a)^2 \hat{\rho}_1 \tag{3.2}$$

$$\nabla \cdot \hat{\mathbf{u}}_1 = 0 \tag{3.3}$$

$$\nabla^2 \hat{\mathbf{u}}_1 - \nabla \hat{p}_1 - \frac{1}{2}(\kappa a)^2 \left(\hat{\rho}_0 \nabla \hat{\phi}_1 + \hat{\rho}_1 \nabla \hat{\phi}_0\right) = 0 \tag{3.4}$$

$$\nabla \cdot \left[ \nabla \hat{n}_{i1} + z_i \left(\hat{n}_{i0} \nabla \hat{\phi}_1 + \hat{n}_{i1} \nabla \hat{\phi}_0\right) - \frac{1}{2} \alpha \hat{n}_{i0} \hat{\mathbf{u}}_1 \right] = 0, \tag{3.5}$$

where dependent variables $\hat{\phi}$, $\hat{n}_i$, $\hat{\mathbf{u}}$, $\hat{p}$ are the dimensionless electric potential, ion number concentration of species *i*, flow velocity, and pressure, respectively. The subscript "0" and "1" correspond to electrostatic and perturbed states, respectively. The dimensionless charge density is defined as $\hat{\rho} = \sum z_i \hat{n}_i = \hat{n}_1 - \hat{n}_2$. Here we use $\phi_c = k_B T / e$, the particle radius *a*, and the bulk concentration $n_\infty$ to scale electric potential, length, ion number concentration, respectively. The velocity is scaled by the electrophoretic velocity $U_c = \varepsilon \phi_c^2 / \eta a$. The pressure is scaled by $p_c = \eta U_c / a$, and the electric force is scaled $F_c = \rho_c a^3 (\phi_c / a) = n_\infty k_B T a^2$. In addition, we define the Péclet number as $\alpha = 2U_c a / D$. The parameters $\varepsilon$, $e$, $k_B$, $T$, $\eta$ correspond to permittivity, electron charge, Boltzmann constant,

temperature, and viscosity, respectively. Proper boundary conditions for both electrostatic and perturbed states are required to solve the complete system.

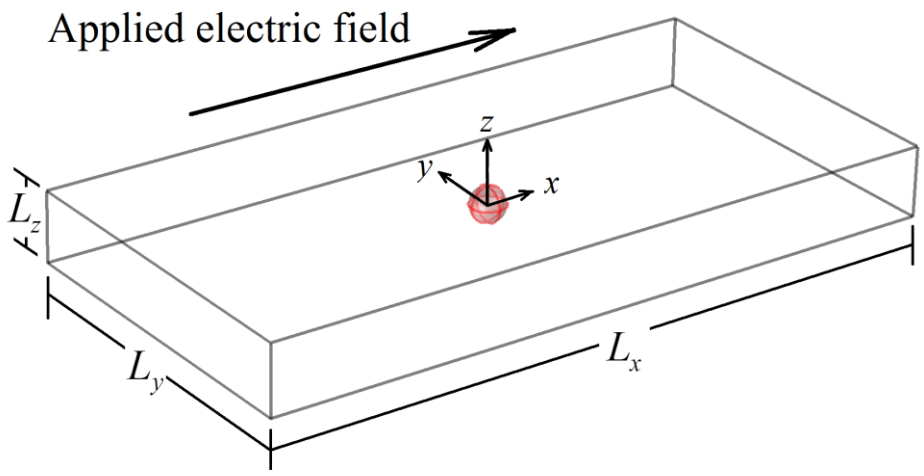


Figure 3.1. Computation domain of our system. The coordinate system is fixed on the particle and the origin is at the center of the particle. We show in Figure 3.6 that the effect of particle location away from the center of the channel is negligible, and therefore this domain is valid in all cases.

### 3.1.2. Boundary Conditions

In our system, the surfaces of the particle and the channel walls are nonconductive and impermeable with a no-slip condition. The coordinates are fixed on the particle, with the origin at the center as shown in Figure 3.1. Zeta potentials are specified at the surfaces of the particle and walls, and we apply constant voltages at both ends of the channel to produce a constant applied electric field along the channel. We fix the coordinates to the particle so that the channel walls are assigned the negative particle velocity. A no stress condition is used at the inlet and outlet far from the particle, where the concentration should reach the equilibrium value. Thus we have the following boundary conditions:

$$\hat{\phi}_0\big|_{\text{particle}} = \hat{\zeta}_p = e\zeta_p / k_B T\,,\ \hat{\phi}_0\big|_{\text{wall}} = \hat{\zeta}_w = e\zeta_w / k_B T\,, \qquad \mathbf{n}\cdot\nabla\hat{\phi}_0\big|_{\text{inlet, outlet}} = 0\,,$$

$$\hat{\phi}_1\big|_{\text{inlet}} = \left(eV_{in} / k_B T\right)/\delta\,, \qquad \hat{\phi}_1\big|_{\text{outlet}} = \left(eV_{out} / k_B T\right)/\delta\,, \qquad \mathbf{n}\cdot\nabla\hat{\phi}_1\big|_{\text{particle, wall}} = 0,$$

$$\hat{\mathbf{u}}_1\big|_{\text{wall}} = \left(-\mathbf{U}_p / U_c\right)/\delta, \qquad \hat{\mathbf{u}}_1\big|_{\text{particle}} = 0, \qquad \mathbf{n}\cdot\left[\nabla\hat{\mathbf{u}}_1 + \left(\nabla\hat{\mathbf{u}}_1\right)^T\right]_{\text{inlet, outlet}} = 0,$$

$$\mathbf{n}\cdot\nabla\hat{n}_{i1}\big|_{\text{particle, wall}} = 0, \qquad \hat{n}_{i1}\big|_{\text{inlet, outlet}} = 0, \tag{3.6}$$

where **n** is the unit normal vector. The applied electric field is specified by $E_\infty = \left(V_{in} - V_{out}\right)/L_x$, where $L_x$ is the distance between the inlet and the outlet.

3.1.3. Calculation of Electric and Hydrodynamic Forces

Equations (3.1)-(3.5) are solved along with the appropriate boundary conditions to find the electrophoretic velocity of the particle under weak applied electric field. Since the unknown nanoparticle velocity is coupled directly to the wall boundary conditions, we vary the particle velocity until the drag force on the particle balances the electric force. For a nonconductive particle surface with specified zeta potential, we apply the simplified electric force expression [48]:

$$\hat{\mathbf{F}}_E = \int \hat{\rho}_s\left(-\nabla\hat{\phi}_1\right)d\hat{A}\,,\ \hat{\rho}_s = -\frac{2}{(\kappa a)^2}\mathbf{n}\cdot\nabla\hat{\phi}_0\,, \tag{3.7}$$

where $\hat{\rho}_s$ is dimensionless surface charge density. In addition, the hydrodynamic force (drag force) on the particle can be obtained by

$$\hat{\mathbf{F}}_D = \frac{2}{(\kappa a)^2}\int\left(\mathbf{n}\cdot\hat{\boldsymbol{\sigma}}\right)d\hat{A}, \tag{3.8}$$

where $\hat{\boldsymbol{\sigma}}$ is the dimensionless fluid stress tensor. Note that a factor $2/(\kappa a)^2$ appears in (3.8) due to the scales used to make the velocity and force nondimensional. After we obtain the equilibrium particle velocity $U_p$, the dimensionless mobility can be calculated by:

$$\hat{\mu} = \frac{\hat{U}_p}{\hat{E}_\infty} = \left(\frac{U_p}{E_\infty}\right) \times \left(\frac{\eta e}{\varepsilon k_B T}\right). \tag{3.9}$$

3.1.4. Numerical Simulation

The equations and associated boundary conditions are solved in a 3D finite element domain using COMSOL V4.4a (*COMSOL, Inc., Stockholm, Se*). Quadratic elements are used for electric potential and ionic potential, and linear elements are used for velocity and pressure fields. The mesh is refined adaptively in the Debye length near the surfaces of the particle and walls. Mesh independence is checked in all cases, and the relative tolerance is chosen to be 0.001.

Our computational domain is a rectangular channel (length $L_x$, width $L_y$, height $L_z$) with a spherical particle as shown in Figure 3.1. Symmetry is used to reduce the computational domain to one-half of the channel. To simulate a practical nanochannel, we consider the confinement effect only in the channel height direction ($L_z = 2h$), while the channel width is computationally chosen to be large, $L_y = 10L_z$, and has negligible influence. The ratio of the channel half height to particle radius is defined as $\hat{h} \equiv h/a$. An electric field of 100 V/m is applied along the channel, and KCl is used as the background electrolyte. Zeta potentials are specified at the surface of the particle and walls, where zero

corresponds to uncharged condition. We use viscosity and permittivity of water at 20°C and assume diffusion coefficient of both $K^+$ and $Cl^-$ to be $1.96\times10^{-9}$ $m^2$ $s^{-1}$ [49].

### *3.2. Particles in Unbounded Domain*

Our full 3D simulation has several advantages. It is applicable to a wide range of parameters and complex geometries. More importantly, we can provide an improved explanation to the nonlinear behavior of mobility by examining directly electric and flow fields near the particle. We first validate our model by comparing to classic models for an unbounded domain [24, 26, 27]. By investigating forces on the particle, we can explain how mobility changes with dimensionless particle zeta potential ($\hat{\zeta}_p$) and dimensionless Debye length ($\hat{\lambda}_D = \lambda_D / a$). Once validated, we use the model to investigate the effect of channel height for both uncharged and charged walls, and determine the relative importance of confinement.

#### 3.2.1. Numerical Model Verification

Figure 3.2 compares normalized mobility $\hat{\mu}_N$ to the results predicted by Henry and Ohshima's theory for low particle zeta potential in an unbounded system [24, 27]. The normalized mobility is defined by:

$$\hat{\mu}_N = \mu / \mu_{Huckel} = \frac{U_p}{E_\infty} / \left( \frac{2\varepsilon\zeta_p}{3\eta} \right). \tag{3.10}$$

Here, wall zeta potential is zero (uncharged) and walls are far from the particle ($\hat{h} = 50$). Therefore the simulation approximates an unbounded system since the influence of the channel walls will be minimal. Specifically, we chose a particle zeta potential of 1 mV

(dimensionless particle zeta potential $\hat{\zeta}_p = 0.04$). Bulk concentration of KCl is varied to alter the EDL thickness around the particle, using the relation $\lambda_D = 1/\kappa = \sqrt{\varepsilon k_B T / 2 n_\infty e^2}$. The good agreement with Henry's function shows our model is accurate over a wide range of bulk electrolyte concentration.

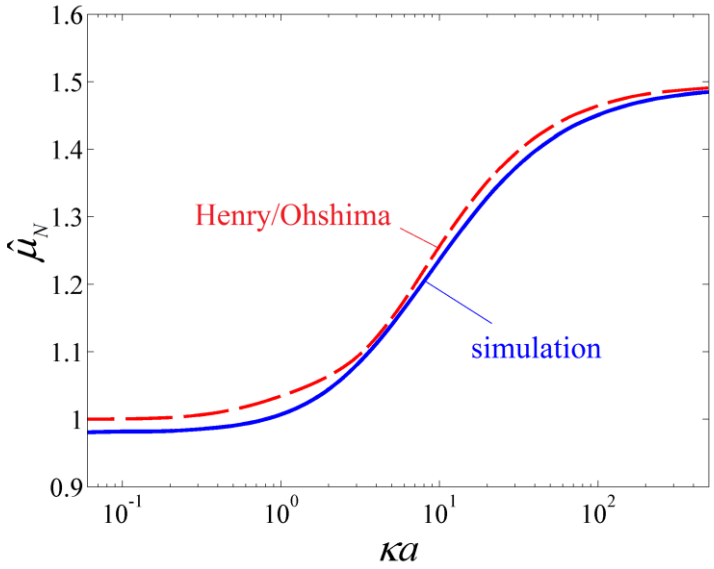


Figure 3.2. Comparison between simulation results and Henry's function [24], showing normalized mobility $\hat{\mu}_N$ from Equation (3.10) as a function of the dimensionless Debye length $\kappa a$. The blue, solid, line is calculated from our simulation, and the red, dashed, line is obtained by Ohshima's expression of Henry's function [27]. The slight deviation (less than 3 %) comes from drag generated by channel walls.

For higher zeta potentials, we compared our results of electrophoretic mobility with literature values [26] in an unbounded domain for both low and high particle zeta potentials. Figure 3.3 shows the dimensionless mobility $\hat{\mu}$ as a function of $\hat{\zeta}_p$ for different values of $\kappa a$. Here we use a 50 nm-diameter particle in a 2.5 μm-wide uncharged channel to minimize

influence of channel walls and to simulate an unbounded environment. Solid lines represent the current simulation, while dashed lines are adopted from O'Brien and White [26]. Note that according to the definition in the literature, the mobility of thick EDL approaches 1 instead of 2/3. Therefore the mobility data from [26] needs to be multiplied by a factor 2/3 to be consistent with our definition of dimensionless mobility. The good agreement indicates that our model correctly captures interactions between electric and flow fields over a wide range of both $\hat{\zeta}_p$ and $\kappa a$.

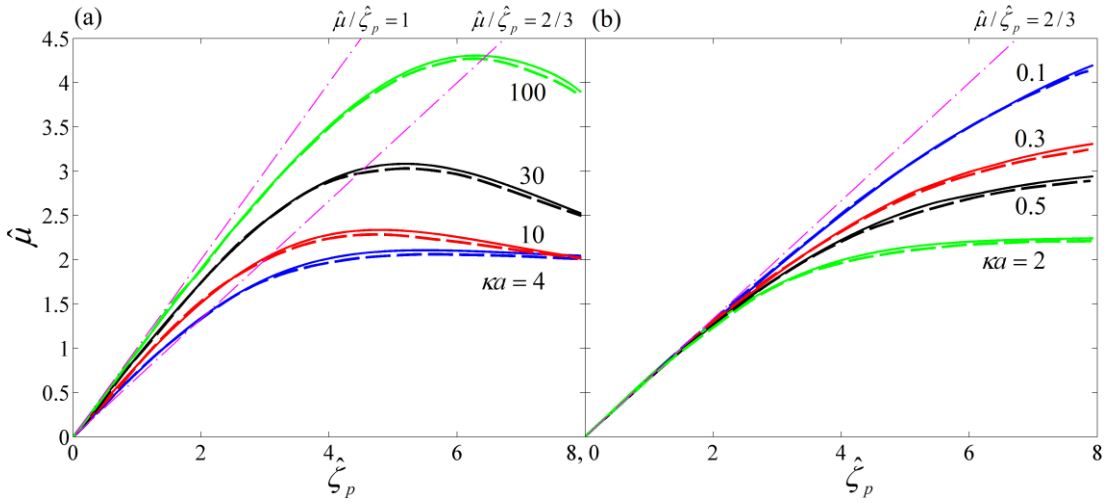


Figure 3.3. Mobility as a function of particle zeta potential with different $\kappa a$ in (a) thin double layer region and (b) thick double layer region. Solid lines are from our simulation and dashed lines are Obrien and White [26]. Two dashed dotted lines correspond to the two limiting cases of thick and thin EDL. Linearity holds for small $\hat{\zeta}_p$ with the slopes bounded by 2/3 and 1. A maximum can only be observed in thin EDL region (a).

### 3.2.2. Nonlinear Behavior of Mobility

In this section, we investigate the behavior of mobility in an unbounded system by examining electric field and ion distribution near the particle. Referring back to Figure 3.3(a)

(thin EDL), at low particle zeta potential, the mobility shows linear dependence on $\hat{\zeta}_p$, and the slopes are bounded by 2/3 and 1, which correspond to Huckel-Onsager and Helmholtz-Smoluchowski's models at thick and thin EDL limits, respectively [22, 23]. However, as $\hat{\zeta}_p$ increases, linearity no longer holds and mobility will reach a maximum, as predicted by O'Brien and White in [26]. Figure 3.3(b) shows mobility in thick EDL systems. Mobility increases linearly only when $\hat{\zeta}_p$ is small as thin EDL case. However, no obvious maximum can be observed in these cases. O'Brien and White suggested that retarding force grows faster with $\hat{\zeta}_p$ than driving force, and consequently maximum mobility exists in thin EDL systems. For the thick EDL case, no maximum appears because the disturbed charge density $\hat{\rho}_1$ is too small to affect retarding force. In our 3D simulation, we can examine in detail the ion distributions around the particle to understand how $\hat{\zeta}_p$ and $\kappa a$ affect forces on the particle as well as the mobility. An example is shown in Figure 3.4.

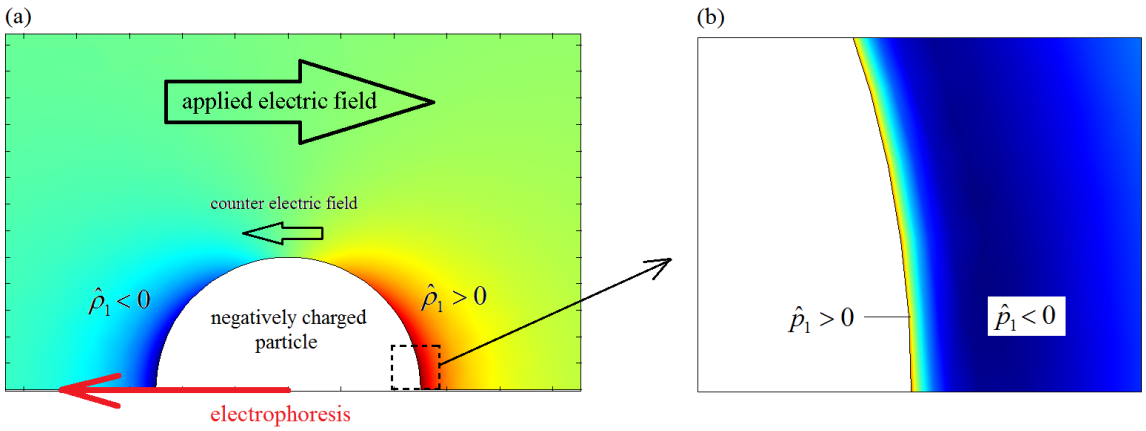


Figure 3.4. The effect of double layer polarization. (a) Distribution of perturbed charge density $\hat{\rho}_1$ is shown near a negatively charged particle. Red and blue colors correspond to positive and negative values, respectively. According to the direction of applied electric field, cations are moved to the front edge of the particle, and a counter electric field is generated to reduce net electric field. Thickness of EDL affects distribution of accumulated ions, which effectively affects counter electric field. (b) We show a zoom-in plot of pressure field at the front edge of the particle. A pressure gradient is formed to balance the electric body force in fluid. As a result the net pressure force acting on the particle is in the same direction as electrophoresis. Note here the color scales are not the same for the two plots.

Specifically, the disturbed counter-ions in diffuse layer will be displaced by the applied electric field. If cations are attracted to a negatively charged particle, for example, the applied electric field will move them toward the front edge of the particle. Therefore positive disturbed charges ( $\hat{\rho}_1 > 0$ ) will be found at the front edge and negative ones at the rear as shown in Figure 3.4(a). This phenomenon is the so-called double layer polarization [11, 13]. Figure 3.4(a) shows a cross sectional plot of distribution of perturbed charge density $\hat{\rho}_1$ near the particle, where the applied electric field is toward right. Red and blue areas correspond to positive and negative values of $\hat{\rho}_1$, respectively.

Double layer polarization induces two major effects. First, the two groups of accumulated charges create a counter electric field against the applied field as shown in Figure 3.4(a), which reduces net electric field near the particle. The counter electric field is affected by charges in the two groups (magnitude of $\hat{\rho}_1$) and the spatial distribution of them (particle geometry and EDL thickness). On the other hand, the accumulated positive charges at the front edge result in a negative electric body force in fluid. To balance it, a pressure gradient toward the particle is built near the front edge, that is, a positive pressure exists at the front surface of the particle as shown in Figure 3.4(b). Similarly a negative pressure acts on the rear surface of the particle. Therefore, a net pressure force toward left (along the direction of electrophoresis) acts on the particle, and it reduces drag force caused by shear stress. Note that the color scales of the two plots are not the same.

Mobility is determined by the magnitude of driving force (electric force) and drag force on the particle. Electric force is proportional to surface charge density and electric field, that is, $\hat{F}_E \sim \hat{\rho}_s \hat{E}$, where $\hat{\rho}_s$ is surface charge density. Surface charge density increases with bulk electrolyte concentration and particle zeta potential, while electric field is reduced by the counter electric field. On the other hand, drag force can be decomposed into skin friction resulting from shear stress and form drag resulting from pressure. Shear stress dominates at high *κa* cases due to the high velocity gradient. However, at low to moderate *κa*, pressure may act against shear stress (due to double layer polarization) to reduce the net drag force. These four terms change with $\hat{\zeta}_p$ and *κa*, and affect mobility in a coupled manner.

### 3.2.3. Particle Zeta Potential

Consider thin EDL systems as shown in Figure 3.3(a). For drag force, shear drag always dominates due to the high velocity gradient. As $\hat{\zeta}_p$ increases, more ions are attracted near the particle and higher electric body force in the fluid causes stronger flow motion. Therefore the net drag force increases with $\hat{\zeta}_p$. On the other hand, the electric force consists of two competing factors: surface charge density $\hat{\rho}_s$ and electric field. From low to moderate $\hat{\zeta}_p$, $\hat{\rho}_s$ increases but electric field decreases due to the counter electric field. As a result, electric force still increases with $\hat{\zeta}_p$. However, the reduction of electric field dominates at high $\hat{\zeta}_p$ and start suppressing electric force. Consequently, drag force grows faster than electric force at high $\hat{\zeta}_p$, which leads to an increasing-decreasing trend in mobility. We also notice that maximal values occur at higher $\hat{\zeta}_p$ as $\kappa a$ increases. A larger value of $\kappa a$ leads to a higher bulk electrolyte concentration and a larger $\hat{\rho}_s$. This indicates that a larger $\hat{\zeta}_p$ is required to generate a larger counter electric field to suppress electric force and mobility, which corresponds to the shift of the maximums.

For thick EDL systems in Figure 3.3(b), a lower value of $\kappa a$ indicates a lower bulk electrolyte concentration and a lower $\hat{\rho}_s$, and reduction of electric field starts dominating at moderate values of $\hat{\zeta}_p$. Therefore, electric force increases first with $\hat{\zeta}_p$ and then decreases. However, pressure is important in thick EDL cases due to moderate shear stress. The magnitude of pressure is comparable to shear stress, but it acts in the opposite direction to reduce net drag force. The effect of double layer polarization is stronger at high $\hat{\zeta}_p$, and it results in greater pressure difference across the nanoparticle and thereby a lower net drag

force. Since the reduction of electric force is compensated by reduction of drag force at high $\hat{\zeta}_p$, mobility shows a monotonic increasing trend in Figure 3.3(b) for thick EDL systems. Note that in Figure 3.3, mobility also changes with *κa*. We will discuss it in next section.

3.2.4. Electrolyte Concentration

To better illustrate the effect of electrolyte concentration, we plot the normalized mobility defined in equation (3.10) as a function of *κa* in Figure 3.5 with different values of $\hat{\zeta}_p$. When $\hat{\zeta}_p$ is 0.04, magnitude of perturbed charge density $\hat{\rho}_1$ is too small to distort the applied electric field (double layer polarization is negligible). Hence mobility agrees with Henry's function as shown in Figure 3.2. However, as $\hat{\zeta}_p$ increases, a minimum normalized mobility exists at moderate *κa*. This can be explained by examining forces on the particle as last section.

Consider a larger value of particle zeta potential ($\hat{\zeta}_p = 2$). For low to moderate *κa*, $\hat{\rho}_s$ increases, but electric field decreases due to the counter electric field. Hence the electric force increases slightly with *κa*. On the other hand, shear stress increases and the importance of pressure decreases due to increasing velocity gradient. Consequently net drag force increases more quickly than the electric force, which leads to decreasing mobility at low *κa* region. For moderate to high *κa*, higher electrolyte concentration indicates higher $\hat{\rho}_s$. In addition, thin EDL confines polarized ions toward the surface of the particle. This reduces the magnitude of counter electric field and thus increases net electric field. Hence, electric force increases drastically with *κa*. For drag force, shear drag dominates and also increases with *κa*. Since electric force increases more quickly at high *κa*, mobility increases for large

$\kappa a$ region. Combining the two parts we can see a decreasing-increasing trend in mobility. If we further increase particle zeta potential ($\hat{\zeta}_p = 4, 8$), increased perturbed charge density $\hat{\rho}_1$ generates higher counter electric field at the same value of electrolyte concentration. This results in lower net electric field and lower electric force on the particle. Therefore a stronger confinement on the polarized ions (thinner EDL, higher $\kappa a$) is required to compensate increment of counter electric field, and the shift of the minimum mobility to higher value of $\kappa a$ can be observed.

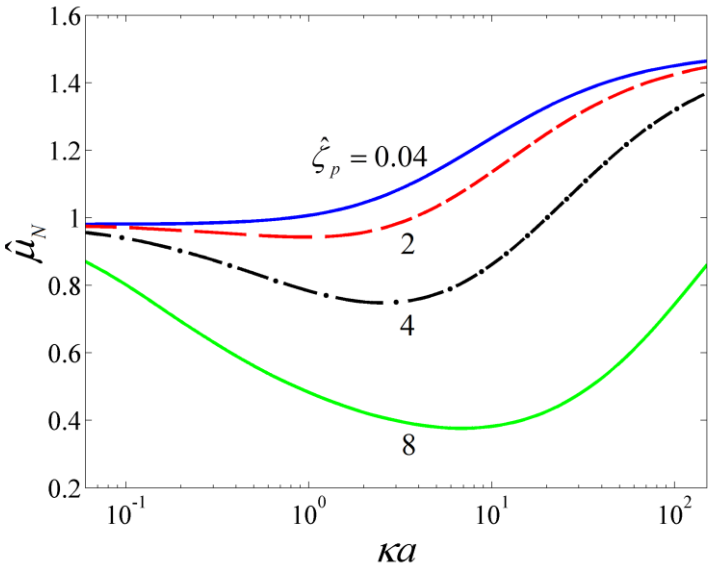


Figure 3.5. Normalized mobility as a function of $\kappa a$ with different particle zeta potential. When $\hat{\zeta}_p$ is small the result agrees with Henry's function. For $\hat{\zeta}_p \geq 2$ minimum mobility occurs at moderate value of $\kappa a$. The location of minimum mobility shifts to higher value of $\kappa a$ as $\hat{\zeta}_p$ increases.

### *3.3. Particles in Confined Channels*

3.3.1. Effect of Particle Location

In order to obtain useful results from simulations with the particle fixed at the center of the channel, it is important to make sure that the effect of the particle being located at various positions across the channel is minimal. For low electrolyte concentrations, we show that the electric double layers are large and confine the particle to the center of the channel. For high electrolyte concentrations, the electric double layers are thinner and the particle position is distributed across the channel. However, even in this case, we can show that the mobility of the particle within this distribution of transverse channel positions varies only by ~1%.

Specifically, in our case the particle and channel walls are both negatively charged, if a particle deviates from the midplane of the channel, it will be repelled due to the electrostatic force. However, this force may be screened at least partially by the EDLs, no matter how thick or thin. Therefore, we calculated the electric force in the transverse direction for different particle locations with different electrolyte concentrations. Figure 3.6 shows the relative electric force as a function of particle location $z_p$ for a 50 nm-diameter and a 10 nm-diameter particle in a 100 nm channel, where $z_p = 0$ corresponds to the nanochannel midplane. The relative electrostatic repulsive force is defined as $\tilde{F}_{e,z} = F_{e,z} / F_{e,x}$, which is a comparison of the cross-channel to the driving electric force. When $\tilde{F}_{e,z} = 1$ the magnitude of the repulsive force is the same as the axial driving force, which means the particle has strong tendency to move towards the midplane. For low electrolyte concentrations (~1 mM) the repulsive force is significant, thereby confining the particle very close to the midplane due to the thick EDLs. In contrast, for high electrolyte concentrations (~3 M), the thin EDLs

effectively screen the repulsive force until the particle is close to the wall. Therefore for high electrolyte concentration (thin EDL) the particle location is distributed across the channel.

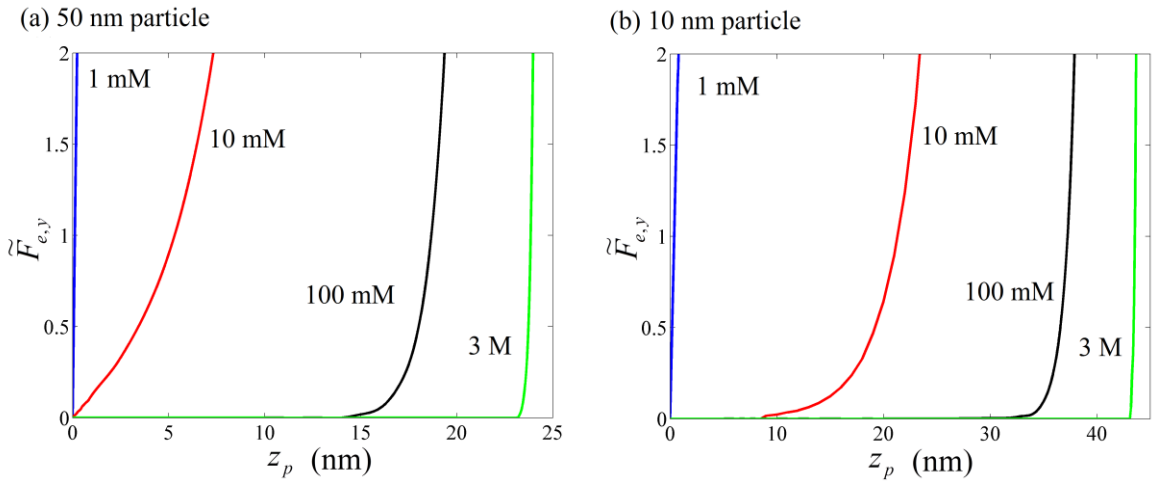


Figure 3.6. Relative electric force as a function of particle location with different electrolyte concentration in a 100 nm channel for (a) a 50 nm-diameter particle and (b) a 10 nm-diameter particle. The repulsive force is strong for low concentration cases even the particle slightly deviates from the midplane.

Subsequently, we focused our attention on the highest electrolyte concentration, 3M, as a worst case scenario where the widest particle distribution occurs. The electrostatic repulsive force distribution is integrated to obtain the energy barrier $U_e$, where $U_e \equiv 0$ at the midplane due to zero repulsive force. In addition, the mobility of the particle is calculated as a function of transverse location. The probability distribution of particle position is related to the energy barrier, $f_Y(y) \sim \exp[-U_e(y)/k_B T]$. The zeta potentials are chosen as $\zeta_p = -1\,\mathrm{mV}$ and $\zeta_w = -2\,\mathrm{mV}$. The average dimensionless mobility for a 50 nm-diameter and a 10 nm-diameter particle is 0.0396 and 0.043, respectively. The mobilities of the two particles at the centerline are 0.0399 and 0.0431, which indicates the deviation is within 1% for both cases.

Since the velocity field generated by electro-osmosis behaves like plug flow, the mobility remains relatively unchanged unless the particle is located near the wall. However, the repulsive force confines the particle near the centerline, which decreases substantially the probability of a particle being located near the wall. Based on these results, we are motivated to restrict our attention to analysis of particle mobility at the channel centerline.

### 3.3.2. Particles in Channels with Uncharged Walls

Here we consider uncharged channel walls, where $\hat{\zeta}_w = 0$. We choose channel heights ranging from 100 nm ($\hat{h} = 2$, nanochannel) to 2.5 μm ($\hat{h} = 50$, microchannel). Figure 3.7 shows mobility as a function of particle zeta potential with different channel heights for thin ($\kappa a = 30$) and thick ($\kappa a = 2$) EDL systems. In both cases the boundary effect seems minor when $\hat{h} > 5$, and the results are similar to those already presented in Figure 3.3. For a bounded domain, linearity at low $\hat{\zeta}_p$ region still holds but confinement effect reduces the slopes due to increased drag. In addition, reduction of mobility is greater for thick EDL systems, because interaction between EDL and channel walls effectively decreases surface charge and electric force on the particle. When $\hat{h}$ drops to 2, the confinement effect is prominent and reduction of mobility could be up to 18% for a thick EDL system. Note that Figure 3.7 can also be interpreted as mobility of particles of different radius in an uncharged nanochannel at a fixed height. Therefore, this shows a possibility of exploiting nanochannels to separate particles of different sizes.

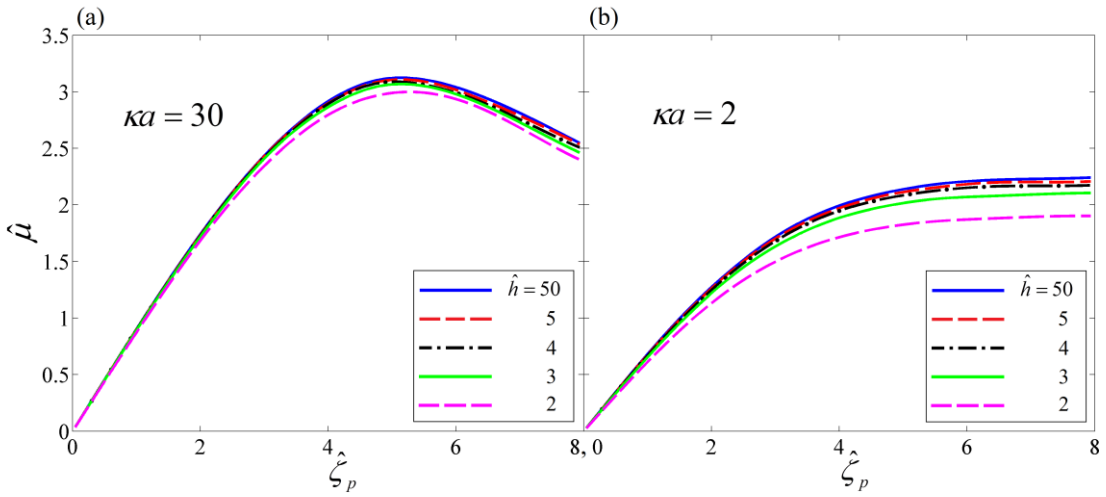


Figure 3.7. Mobility as a function of particle zeta potential with channel heights for (a) $\kappa a$ = 30 and (b) $\kappa a$ = 2. Confinement effect is not important when $\hat{h}$ > 5. Linearity still holds at low $\hat{\zeta}_p$ , while the slope reduces for narrow channels due to increased drag. Reduction of mobility is prominent for $\hat{h}$ = 2 especially at low value of $\kappa a$, which is due to interaction between EDL and channel walls.

### 3.3.3. Particles in Channels with Charged Walls

In particle mobility experiments, particle total mobility can be divided into electrophoretic and electro-osmotic components, which are usually treated independently [38, 39]. However, EDLs generated by the particle and by channel walls interact with each other, which affects mobility especially when channel height is comparable to thickness of EDL. Therefore, particle mobility should in fact deviate from that predicted by superposition of electrophoretic and electro-osmotic mobility. Further restricting our attention to a 50 nm-diameter particle, Figure 3.8 shows particle total mobility from numerical simulation as a function of $\kappa a$ for $\hat{h}$ = 50 and 2. This result is compared to total mobility obtained by superimposing electrophoretic and electro-osmotic mobility ($\hat{\mu}_{total} = \hat{\mu}_{EP} - \hat{\mu}_{EOF}$ as in classical models), using the classic expression $\hat{\mu}_{EOF} = \hat{\zeta}_w$ to calculate electro-osmotic flow.

The particle and walls are assumed to be negatively charged to simulate practical conditions, and values of zeta potential are chosen as $\hat{\zeta}_p = \hat{\zeta}_w = -0.04$ to avoid any nonlinear effects caused by double layer polarization. For thin EDL systems in a large channel ($\hat{h}$ = 50), the results from superposition are valid, since no interaction occurs between the EDLs of the channel walls and the particle. However, as *κa* decreases, the EDLs overlap, and lead to a moderate deviation at thick EDL region.

When the channel height further reduces ($\hat{h}$ = 2), deviation in mobility exists even for thin EDLs. This indicates that charged walls influence the confinement effect by increasing hydrodynamic drag. Near the thick EDL limit, on the other hand, a significant deviation can be observed. The speed of background flow (electro-osmosis) is strongly suppressed by overlapping EDLs, which provides a lower magnitude of $\hat{\mu}_{EOF}$ compared to the expression ($\hat{\mu}_{EOF} = \hat{\zeta}_w$) used in the superposition method. Therefore, the total mobility calculated by superposition overpredicts mobility. Given the influence of overlapping EDLs on electrophoresis and electro-osmosis, we conclude that incorporating both effects simultaneously is required in order to accurately predict the mobility of a particle in a nanochannel.

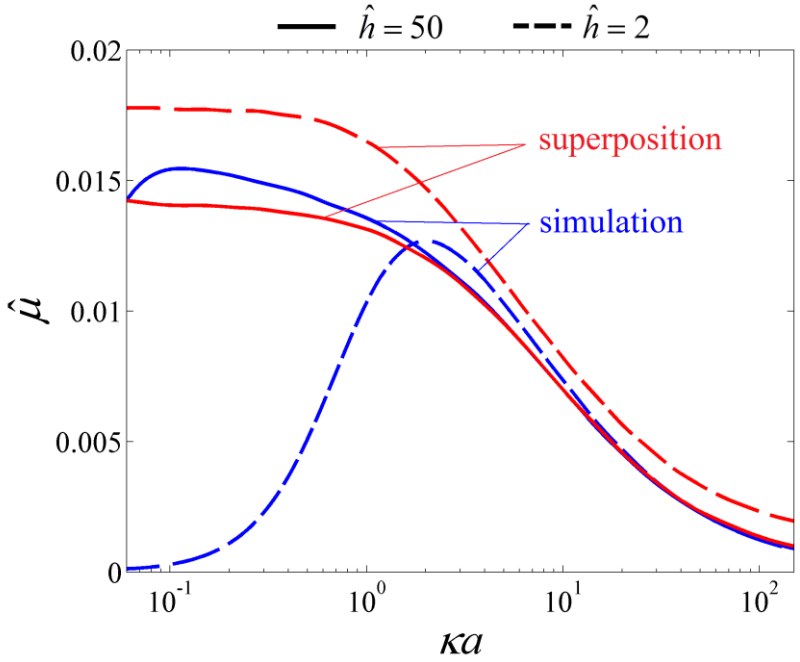


Figure 3.8. Particle total mobility as a function of $\kappa a$ with different channel heights from direct simulation and superposition of electrophoresis and electro-osmosis. Solid lines and dashed lines correspond to $\hat{h} = 50$ and $\hat{h} = 2$, respectively. Good agreement can be found at large $\kappa a$ for $\hat{h} = 50$. As $\kappa a$ decreases, EDL overlapping happens and mobility is overpredicted by superposition. In addition, deviation at high value of $\kappa a$ can also be observed in $\hat{h} = 2$ case, which is due to modification of shear drag generated by walls.

Figure 3.9 shows total mobility verses $\kappa a$ for two different size channels (solid lines for $\hat{h} = 50$, dashed lines for $\hat{h} = 2$). The value of wall zeta potential $\hat{\zeta}_w$ is fixed at -0.08, and particle zeta potential $\hat{\zeta}_p$ is chosen as -0.04, -0.08, and -0.12. First, in the thin EDL regime ($\kappa a > 100$), there is no interaction between EDLs from the particle and walls. The Helmholtz-Smoluchowski model is valid and total mobility can be approximated by superposition of electrophoretic and electro-osmotic mobility, that is, $\hat{\mu}_{total} \approx \hat{\mu}_{EP} - \hat{\mu}_{EOF} = \left(\hat{\zeta}_p - \hat{\zeta}_w\right)$. Note that both the particle and walls are negatively charged,

and consequently electrophoresis is in the opposite direction to electro-osmosis. For example, if $\hat{\zeta}_p$ = -0.12, electrophoretic mobility dominates and the particle moves against direction of the background EOF flow ( $\hat{\mu}_{total} < 0$).

The deviation in mobility between the two channel heights depends on the value of $\left(\hat{\zeta}_p - \hat{\zeta}_w\right)$ at the thin EDL limit. In the case of $\hat{\zeta}_p = \hat{\zeta}_w$ = -0.04, mobility approaches zero for both channel heights, and the confinement effect is not observed. This is due to the charged condition at the wall surfaces. Specifically, electro-osmotic flow generated in thin EDL systems can be interpreted as a shear flow, which superimposes shear drag on the particle. In this case, the velocity near the walls has the same magnitude and direction as velocity near the particle. Consequently, no shear stress from the walls can be perceived by the particle, which effectively eliminates the confinement effect. Similarly, if flow near the walls is faster, for example in the $\hat{\zeta}_p$ = -0.04 case, the shear stress acts on the particle along the direction of electrophoresis and increases electrophoretic mobility, which results in a lower total mobility. Since shear stress depends on the velocity gradient, this effect is predominant for small channel heights. The results suggest that particle mobility can be altered by using different materials or surface coatings for nanochannels.

As $\kappa a$ decreases ($\lambda_D$ increases), $\hat{\mu}_{total}$ increases due to decreased $\hat{\mu}_{EP}$. As the EDL thickness increases, the wall EDLs will increasingly interact with the particle EDLs. This reduces surface charge density on the particle, which reduces $\hat{\mu}_{EP}$. In addition, the magnitude of $\hat{\mu}_{EOF}$ remains constant, since the EDLs from the top and bottom walls do not overlap. Subsequently, total mobility continues to increase with decreasing $\kappa a$. As $\kappa a$ decreases even further, the EDLs from the top and bottom walls start to interact, thereby

reducing the electro-osmotic flow, as observed in Figure 3.9. Overlapping can occur for large EDL thicknesses, even in relatively large channels. Consequently, the maximum mobility appears at lower $\kappa a$ for $\hat{h} = 50$.

As $\kappa a$ approaches zero (thick EDL limit), electro-osmotic mobility approaches zero due to extremely low charge density in flow. In this case, particle total mobility is dominated by electrophoretic mobility. According to Huckel-Onsager's model, the drag force on the particle can be predicted by Stokes' law (with modification to include channel walls). In addition, since $\kappa a$ approaches zero, the Poisson-Boltzmann equation (3.1) reduces to Laplace's equation. With specified zeta potential at the particle and walls, surface charge density of the particle should be proportional to the difference in the zeta potentials. The electric force as well as total particle mobility should proportional to $(\hat{\zeta}_p - \hat{\zeta}_w)$ near the thick EDL limit.

At low $\kappa a$, the effect of EDL overlapping leads to significant differences in mobility. The mobility of a nanoparticle in a nanochannel is greater than that in a microchannel at moderate $\kappa a$. Finally, when magnitude of particle zeta potential is higher ($\hat{\zeta}_p$ = -0.12), mobility changes from negative to positive value, and then back to negative again. The results indicate that particle motion can be manipulated by changing electrolyte concentration in a nanochannel.

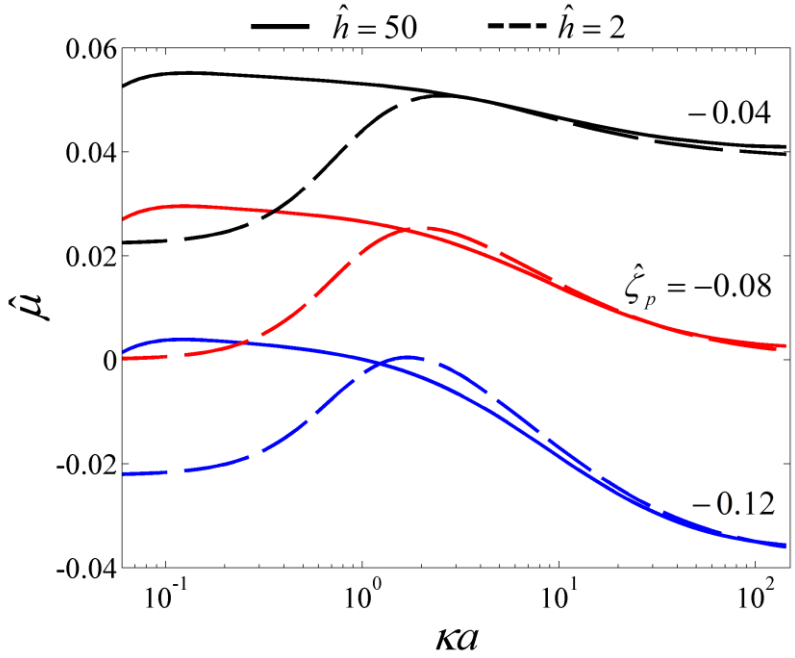


Figure 3.9. Total mobility as a function of *κa* with different values of $\hat{\zeta}_p$ and channel height. At the region of high *κa* mobility approaches a proportional difference of $\hat{\zeta}_p$ and $\hat{\zeta}_w$, which can be predicted by Helmholtz-Smoluchowski model. As *κa* decreases, the thickness of the EDL increases and starts overlapping, which leads to increasing-decreasing behavior of mobility. As *κa* approaches zero, Huckel-Onsager model is applicable but corrections need to be made to account for effects of finite $\hat{\zeta}_w$ and confinement.

### 3.3.4. Application to Nanochannels

In the above sections we showed that particle mobility is affected by particle zeta potential, electrolyte concentration, channel size, and wall zeta potential. However, particle zeta potential and electrolyte concentration cannot be arbitrarily specified in real applications. Consequently, particle mobility can be manipulated by choosing channels with different heights or surface charges [50]. For example, if the value of wall zeta potential is chosen between the values of particle zeta potential of two types of particles, the two particle types will migrate in the opposite directions under an applied electric field. The results

shown in Figure 3.9 can also be viewed as particle mobilities with different sizes in the same charged channel. For example, consider two particle types: 50 nm-diameter and 10 nm-diameter. Figure 3.10 shows particle mobility as a function of electrolyte concentration in a microchannel and a nanochannel. The zeta potentials are chosen as $\hat{\zeta}_p$ = -0.04, $\hat{\zeta}_w$ = -0.08. Figure 3.10 indicates how nanochannels (dashed lines) can be used to separate 10 and 50 nm diameter particles using 1 μM - 1 M electrolyte concentrations, with a significant improvement being observed at the lower and higher electrolyte concentration regions. The microchannels (solid lines) can separate the two types of particles, but only for higher electrolyte concentrations. This indicates that one can exploit nanochannels to separate particles efficiently over a large range of electrolyte concentrations.

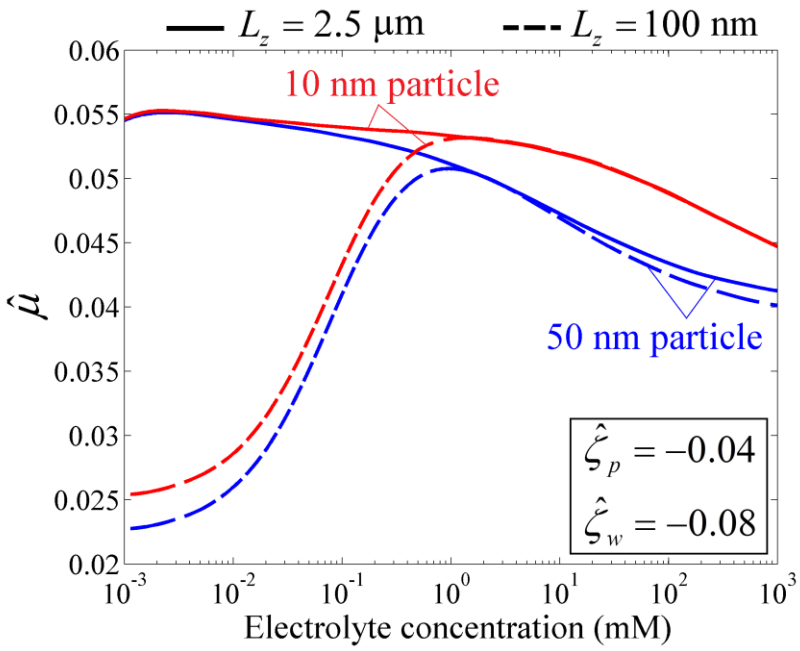


Figure 3.10. Mobility as a function of electrolyte concentration of 10 nm and 50 nm particles. Solid lines and dashed lines correspond to results in a microchannel and a nanochannel, respectively. Difference in mobility shows ability of separation, and no significant improvement is observed in a nanochannel.

The conventional method to estimate particle zeta potential incorporates Helmholtz-Smoluchowski's model and electrophoretic mobility, which is calculated by subtracting particle total mobility from the electro-osmotic mobility. As discussed above, this approach fails for cases with thick EDLs or with high particle zeta potentials. In addition, the difference between total mobility and electro-osmotic mobility is relatively small, and can introduce significant error. Subsequently, we propose here a new method for estimating particle and wall zeta potentials by using only the total particle mobility as measured in two different height channels. Figure 3.11 shows contours of total particle mobility as a function of $\hat{\zeta}_p$ and $\hat{\zeta}_w$ with 1 mM electrolyte concentration ($\kappa a$ = 2.61) for $\hat{h}$ = 50 (solid lines) and $\hat{h}$ = 2 (dashed lines). Numbers on contour lines correspond to dimensionless total particle mobility. Once the total particle mobility has been measured in the two different height channels, the intersection of corresponding contours leads to definitive values of particle and wall zeta potentials.

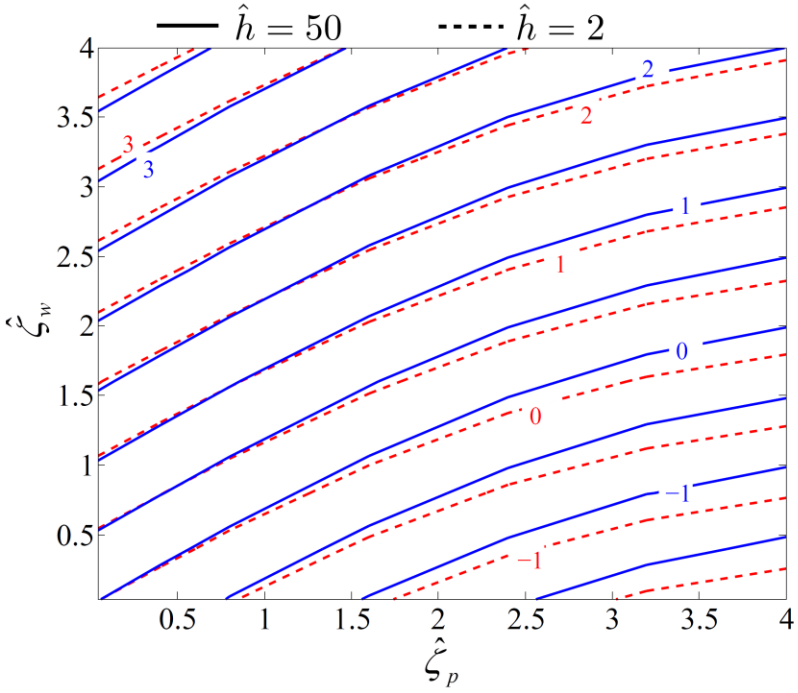


Figure 3.11. Contours of total particle mobility as a function of $\hat{\zeta}_p$ and $\hat{\zeta}_w$ with $\kappa a$ = 2.61. Solid and dashed lines correspond to $\hat{h}$ = 50 and 2, respectively. Using mobility measurements obtained using the two different height channels, particle and wall zeta potentials can be determined by the intersection of corresponding contours.

For example, if we want to determine the zeta potential of a 50 nm-diameter particle, we can measure its mobility in a 2.5 μm-high channel ($\hat{h}=50$) and a 100 nm-high channel ($\hat{h}=2$) filled with 1 mM KCl solution ($\kappa a$ = 2.61). For demonstration purposes, let's assume that the measured total particle mobilities are, say, $\mu_{\hat{h}=50}=1$ and $\mu_{\hat{h}=2}=1$. Then by comparing the measured mobilities with Figure 3.11, we can estimate that the particle and channel zeta potentials are 19.8 mV ($\hat{\zeta}_p$ = 0.792) and 39.8 mV ($\hat{\zeta}_w$ = 1.59), respectively. If the error from mobility measurement is, say, 3%, the error for zeta potential would also be about 3%. Our approach can avoid the errors generated from measuring electro-osmotic

mobility, and works for a wide range of $\kappa a$ and $\hat{\zeta}_p$. Note that Figure 3.11 is restricted to the value $\kappa a = 2.61$. This approach can be readily extended for other values of $\kappa a$.

# 4. Electromigration of 2D Nanorods in Nanochannels

In this chapter we improve our steady-state model to include fluid-structure interaction. The new model is used to track motion of nanorods in nanochannels. The confinement of nanocahnnel can be observed for lower electrolyte concentration due to interaction of thick EDLs. Particle mobility is calculated in both models to determine when the steady-state model would be a good approximation.

## *4.1. Equations and Numerical Simulation*

### 4.1.1. Governing Equations

Consider a rod particle in a two-dimensional channel filled with KCl electrolyte solution, as shown in Figure 4.1. The flow is assumed to be incompressible due to low Reynolds number flow in nano-confined channels. Following our previous work in chapter 2, for an applied electric field, the dimensionless governing equations can be written as electrostatic and perturbed equations as follows:

$$\nabla^2\hat{\phi}_0 = (\kappa a)^2 \sinh\hat{\phi}_0, \tag{4.1}$$

$$\nabla^2\hat{\phi}_1 = -\frac{1}{2}(\kappa a)^2 \hat{\rho}_1, \tag{4.2}$$

$$\nabla\cdot\hat{\mathbf{u}}_1 = 0, \tag{4.3}$$

$$\nabla^2\hat{\mathbf{u}}_1 - \nabla\hat{p}_1 - \beta\left(\hat{\rho}_0\nabla\hat{\phi}_1 + \hat{\rho}_1\nabla\hat{\phi}_0\right) = 0, \tag{4.4}$$

$$\nabla\cdot\left[\nabla\hat{n}_{i1} + z_i\left(\hat{n}_{i0}\nabla\hat{\phi}_1 + \hat{n}_{i1}\nabla\hat{\phi}_0\right) - \frac{1}{2}\alpha\hat{n}_{i0}\hat{\mathbf{u}}_1\right] = 0, \tag{4.5}$$

where $\hat{\phi}$, $\hat{n}_i$, $\hat{\mathbf{u}}$, $\hat{p}$, $\hat{\rho}$ are the dimensionless electric potential, ion number concentration of species *i*, flow velocity, pressure, and charge density, respectively. The subscript "0" and "1" correspond to electrostatic and perturbed states, respectively. The electrostatic ion concentration follows Boltzmann distribution, that is, $\hat{n}_{i0} = \exp\left(-z_i \hat{\phi}_0\right)$. Here we use $\phi_c = k_B T / e$, the particle radius *a*, and the bulk concentration $n_\infty$ to scale electric potential, length, ion number concentration, respectively. The velocity is scaled by the electrophoretic velocity, $U_c = \varepsilon \zeta E_\infty / \eta$, and pressure is scaled by $p_c = \eta U_c / a$. The reciprocal Debye length is defined as $\kappa = 1/\lambda_D = \left(2 n_\infty e^2 / \varepsilon k_B T\right)^{1/2}$, and $\beta = n_\infty k_B T a^2 / \eta U_c a$ represents the ratio of electric force scale to hydrodynamic force scale. In addition, we define the ion Péclet number as $\alpha = 2 U_c a / D$. The parameters $\varepsilon$, $e$, $k_B$, $T$, $\eta$, $D$, $\zeta$, $E_\infty$ correspond to permittivity, electron charge, Boltzmann constant, temperature, viscosity, ion diffusion coefficient, zeta potential, and applied electric field, respectively.

To simulate a moving particle in a channel, we consider the fluid-structure interaction between the solid particle and the fluid. Here we consider a homogeneous, isotropic and linear elastic solid particle. Without body force, the displacement of the particle is governed by

$$\nabla \cdot \hat{\boldsymbol{\sigma}}_{solid} = 0, \tag{4.6}$$

$$\hat{\boldsymbol{\sigma}}_{solid} = \hat{J}^{-1} \hat{\mathbf{F}} \hat{\mathbf{S}}_{solid} \hat{\mathbf{F}}^T, \qquad \hat{\mathbf{F}} = \mathbf{I} + \nabla \hat{\mathbf{u}}_{solid}, \qquad \hat{J} = \det \hat{\mathbf{F}}, \tag{4.7}$$

$$\hat{\boldsymbol{\varepsilon}}_{solid} = \frac{1}{2}\left[\nabla \hat{\mathbf{u}}_{solid} + \left(\nabla \hat{\mathbf{u}}_{solid}\right)^T + \left(\nabla \hat{\mathbf{u}}_{solid}\right)^T \nabla \hat{\mathbf{u}}_{solid}\right], \tag{4.8}$$

$$\hat{S}_{solid,ij} = \hat{\lambda} \hat{\varepsilon}_{solid,kk} \delta_{ij} + 2 \hat{G} \hat{\varepsilon}_{solid,ij}, \tag{4.9}$$

where $\hat{\boldsymbol{\sigma}}_{solid}$ and $\hat{\mathbf{S}}_{solid}$ are Cauchy stress and second Piola–Kirchhoff stress. $\hat{\mathbf{u}}_{solid}$ is the deformation of the solid particle, while $\hat{\mathbf{F}}$ and $\hat{\boldsymbol{\varepsilon}}_{solid}$ are deformation gradient and Lagrangian finite strain tensor. $\hat{\lambda} = \lambda/(\eta U_c / a)$ and $\hat{G} = G/(\eta U_c / a)$ are the scaled Lame constant and shear modulus, respectively, which are related to Young's modulus and Poisson's ratio by $E = G(3\lambda + 2G)/(\lambda + G)$ and $\nu = \lambda / 2(\lambda + G)$. We assume the density of the particle is roughly the same as the flow [51], so the inertial term can be neglected due to small Reynolds number. Proper boundary conditions for both electrostatic and perturbed states are required to solve the complete system of equations (4.1)-(4.9).

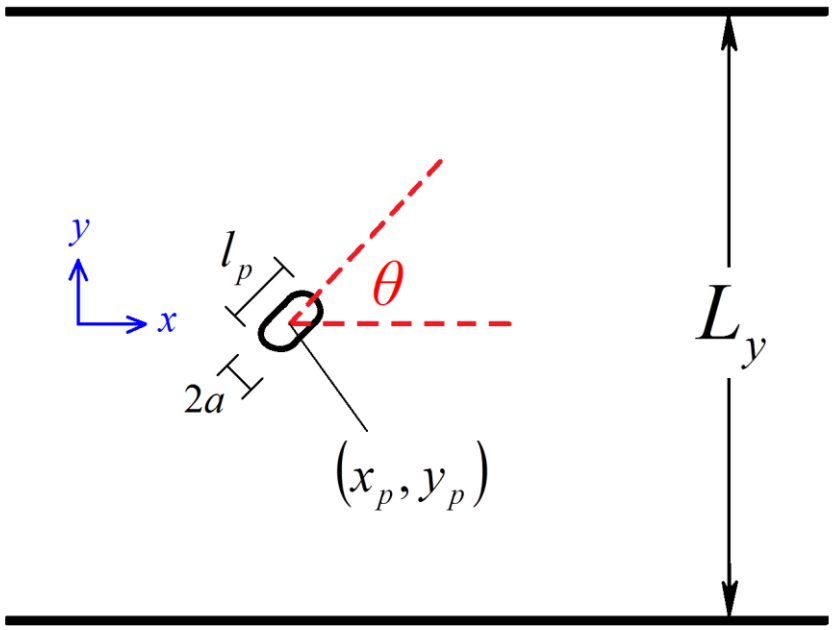


Figure 4.1. Computational domain of two-dimensional rod-like particle flowing through a two-dimensional channel. The angle of the particle is defined as the angle between the major axis of the particle and *x*-axis. A $2a \times l_p$ rod with semicircle ends is used in the simulations. The center of the particle is located at $(x_p, y_p)$, and the channel height is $L_y$.

4.1.2. Boundary Conditions

In our system, the surfaces of the particle and the channel walls are nonconductive and impermeable. Constant surface charge density is specified at the surfaces of the particle and walls, and we apply constant voltages at both ends of the channel to produce an applied electric field along the channel. Surface charge density can be related to zeta potential by $\rho_s = \varepsilon\zeta\kappa$ for small surface charge [52], which is a good approximation when $\zeta < k_B T / e \approx 25$ mV at room temperature. To increase the duration of simulation, we chose a reference frame traversing with a velocity close to the particle streaming velocity. The velocity and normal stress of the fluid and the solid are matched at the solid-fluid interface. In addition, an electric force is exerted on the surface of the particle by the applied electric field. No stress condition is used at the inlet and outlet far from the particle, where the concentration should reach the equilibrium value. Thus we have the following boundary conditions:

$$\mathbf{n}\cdot\nabla\hat{\phi}_0\big|_{\text{particle}} = -(\kappa a)^2\hat{\rho}_{s,p}/2,\ \mathbf{n}\cdot\nabla\hat{\phi}_0\big|_{\text{wall}} = -(\kappa a)^2\hat{\rho}_{s,w}/2, \qquad \mathbf{n}\cdot\nabla\hat{\phi}_0\big|_{\text{inlet, outlet}} = 0,$$

$$\hat{\phi}_1\big|_{\text{inlet}} = (eV_{in}/k_BT), \qquad \hat{\phi}_1\big|_{\text{outlet}} = (eV_{out}/k_BT), \qquad \mathbf{n}\cdot\nabla\hat{\phi}_1\big|_{\text{particle, wall}} = 0,$$

$$\hat{\mathbf{u}}_1\big|_{\text{wall}} = (-\mathbf{U}_w/U_c), \qquad \hat{\mathbf{u}}_1\big|_{\text{particle}} = \frac{\partial\hat{\mathbf{u}}_{solid}}{\partial\hat{t}}, \qquad \mathbf{n}\cdot\hat{\boldsymbol{\sigma}}\big|_{\text{inlet,outlet}} = 0,$$

$$\mathbf{n}\cdot\nabla\hat{n}_{i1}\big|_{\text{particle, wall}} = 0, \qquad \hat{n}_{i1}\big|_{\text{inlet, outlet}} = 0, \qquad \mathbf{n}\cdot\hat{\boldsymbol{\sigma}}_{solid}\big|_{\text{particle}} = \mathbf{n}\cdot\hat{\boldsymbol{\sigma}} - \beta\hat{\rho}_{s,p}\nabla\hat{\phi}, \quad (4.10)$$

where $\mathbf{n}$ is the unit normal vector, and $\hat{\rho}_{s,p}$, $\hat{\rho}_{s,w}$ are dimensionless particle and wall surface charge density. The applied electric field is specified by $E_\infty = (V_{in} - V_{out})/L_x$, where $L_x$ is the

distance between the inlet and the outlet. Here $\hat{\boldsymbol{\sigma}} = \left[ -\hat{p}_1 \mathbf{I} + \left( \nabla \hat{\mathbf{u}}_1 + (\nabla \hat{\mathbf{u}}_1)^T \right) \right]$ is the dimensionless flow stress.

4.1.3. Numerical Simulation

The equations and associated boundary conditions are solved in a 2D finite element domain using COMSOL V4.4a (*COMSOL, Inc., Stockholm, Se*). Quadratic elements are used for electric potential and ionic potential, and linear elements are used for velocity, pressure, and displacement. The mesh is refined adaptively near the surfaces of the particle and walls. Mesh independence is checked in all cases, and the relative tolerance is chosen to be 0.001.

Our computational domain is a rectangular channel (length $L_x$, height $L_y$) with a rod-like particle as shown in Figure 4.1. The 2D rod has 2 nm diameter and 3.4 nm height with round ends, and the channel height is chosen as 100 nm ($\hat{L}_y$ = 100). An electric field of 1000 V/m is applied along the channel. The surface charge density at the walls is specified as $\rho_{s,w} = -7.31 \times 10^{-5}\ \mathrm{C/m^2}$, which corresponds to zeta potential $\zeta_w = -2\ \mathrm{mV}$. The surface charge density of the particle is chosen as $\rho_{s,p} = 0.5\rho_{s,w}$. We use viscosity and permittivity of water at 20°C and assume diffusion coefficient of both $K^+$ and $Cl^-$ to be $1.96 \times 10^{-9}\ \mathrm{m^2\ s^{-1}}$ [49].

The arbitrary Lagrangian-Eulerian method (ALE) [53, 54] is used to deal with the moving particle-fluid interface. The mesh deforms to capture the motion of the particle until the quality of mesh degrades to a specified isochoric distortion level. Then an undeformed mesh corresponded to the new deformed geometry is created and the similar approach is

repeated. This method is widely used in tracking particle motion over an extended period of time.

### *4.2 Results and Discussions*

#### 4.2.1. Particle Trajectory

In our initial simulations, the nanorod is located near the bottom wall at $\hat{y}_0 = -30$ with an inclination angle, $\theta_0 = 30°$. Figure 4.2 shows the representative particle motion over 8000 non-dimensional time steps, with two electrolyte concentrations 1 mM ($\hat{\lambda}_D$ = 9.57), and 10 mM ($\hat{\lambda}_D$ = 3.03). For the 1 mM case, the particle moves toward the centerline and is confined with the major axis parallel to the applied electric field. This is because the thick EDLs, the strong repulsive forces repel the negatively charged particle away from the negatively charged walls, and orientate the particle to align horizontally with the flow direction.

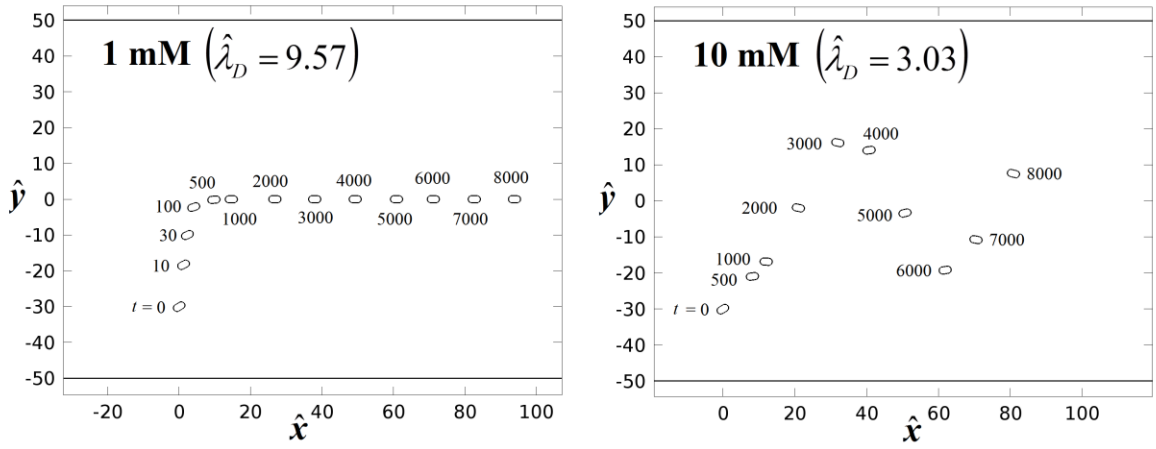


Figure 4.2. Particle trajectories from $\hat{t}$ = 0 to 8000 in a 100 nm height nanochannel for (a) 1 mM electrolyte concentration and (b) 10 mM electrolyte concentration. The particle is confined at the centerline for 1 mM case because of the thick EDLs. For the 10 mM case, when the particle moves toward the top wall, the velocity is decreased by the increased repulsive force, and eventually moves in the opposite direction. The particle repeatedly oscillates, and the trajectory behaves similar to a sinusoid.

For the 10 mM case, the particle tends to move towards the centerline. However, it overshoots the centerline continually. Around $\hat{t}$ = 2000, the particle moves past the centerline and towards the top wall. When the particle is close to the top wall, the transverse velocity is decreased by the repulsive force, and eventually turns toward the centerline again. In this case, the particle moves in an oscillatory manner in a confined region of the channel. Because of the relatively thin EDLs that screen charges, the particle does not feel the repulsive force of the EDL unless it is near the walls. Therefore, the particle is confined towards the center region of the channel, while the angle of the particle changes continually as the particle travels through the channel. Clearly, the degree of particle confinement is strongly affected by electrolyte concentration. A similar conclusion was obtained in the steady-state model by calculating the transverse force on the particle [45].

To better visualize the behavior of the particle in different electrolyte concentrations, the transverse location $\hat{y}_p$ at the center of the particle is plotted as a function of time in Figure 4.3. During 20000 non-dimensional time steps, the particle stays at the centerline for 1 mM case, while it never moves outside $-30 < \hat{y} < 30$ region for 10 mM case. This is because the interaction of the fluid and the nonsymmetrical rod-shape particle causes a nonzero transverse force and moment, which results in the particle transverse motion as well as rotation, an effect that is not captured by any steady state model.

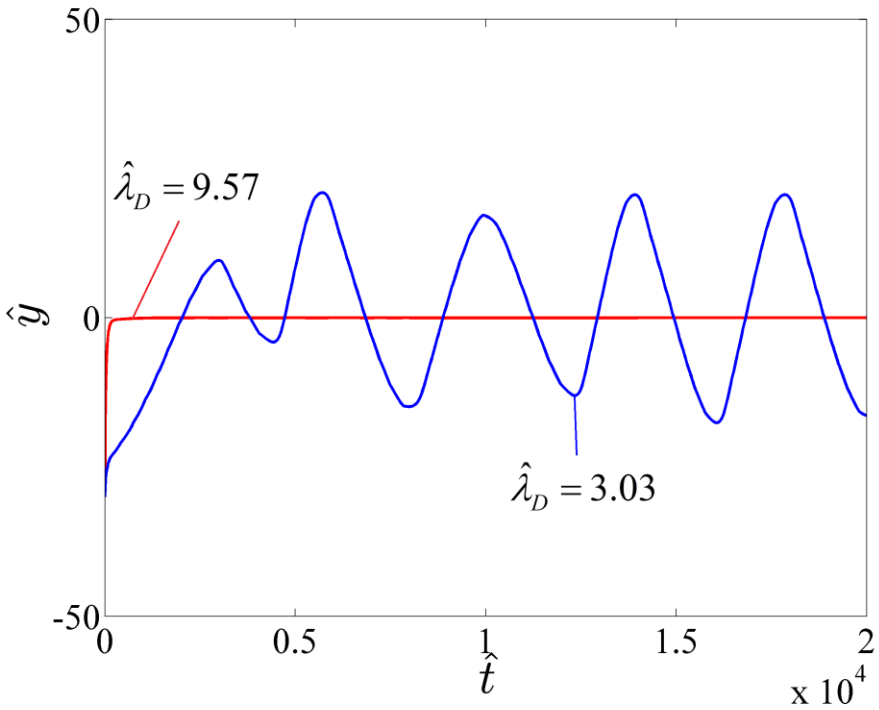


Figure 4.3. Particle transverse location as a function of time with 1 mM ($\hat{\lambda}_D$ = 9.57) and 10 mM ($\hat{\lambda}_D$ = 3.03) electrolyte concentration for a cylindrical particle. The particle is confined at the centerline for the 1 mM case, while the particle moves in an oscillatory manner inside $-30 < \hat{y} < 30$ region for the 10 mM case due to the interaction of EDLs of the particle and walls.

For the 1 mM case, the initial angular position of the particle does not affect the resulting particle trajectory, because the strong confinement forces the particle to move along the centerline, independent of initial position. However, the particle motion could possibly be dependent upon initial positions for thinner EDL cases. Four simulations were performed for a rod with two different initial positions and two different initial angles for the case of 10 mM electrolyte concentration. The simulated transverse locations are shown in Figure 4.4 for these four cases. Note that the initial conditions only affect the particle motion during the initial transient stage ($\hat{t} < 5000$). For larger times, all the cases reported here show similar oscillatory movement and have nearly identical mobilities (the differences are less than 2%). Therefore, one can conclude that the initial conditions of the particle are not substantially important for the current study.

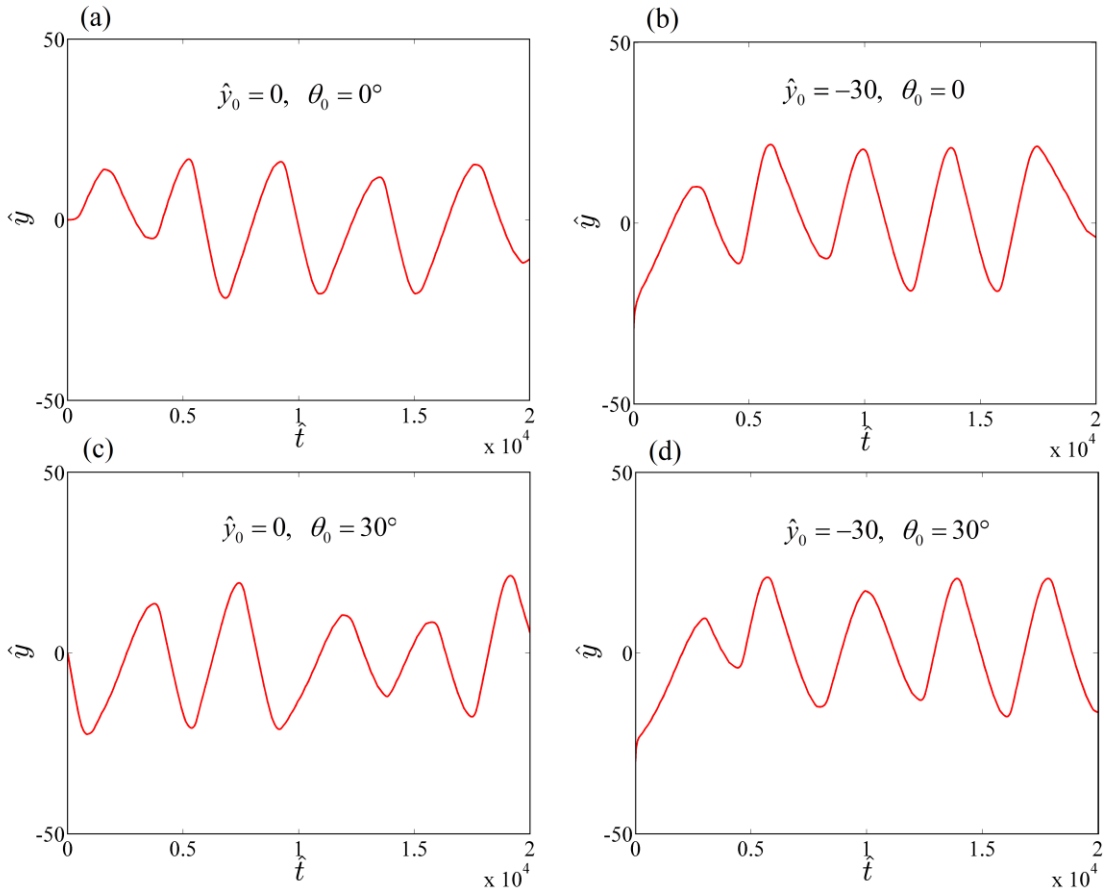


Figure 4.4. Particle transverse location as a function of time with 10 mM electrolyte concentration for different initial conditions: (a) $\hat{y}_0$ = 0, $\theta_0$ = 0. (b) $\hat{y}_0$ = -30, $\theta_0$ = 0. (c) $\hat{y}_0$ = 0, $\theta_0$ = 30°. (d) $\hat{y}_0$ = -30, $\theta_0$ = 30°. After 5000 time steps the particle motion is independent of the initial conditions. The particle has oscillatory motion in the same confined region with the same mobility in flow direction.

Figure 4.4(c) indicates that an unstable equilibrium state exists at $\left(\hat{y}_p = 0, \quad \theta = 0\right)$. A small disturbance can cause small nonzero transverse forces that initiate transverse motion and rotation. In our simulation, the disturbance comes from the numerical error, while in reality it is generated by Brownian motion. Therefore, the particle will never stay at the centerline unless it is under complete EDL-induced confinement.

Figure 4.5 shows the transverse location of the particle as a function of time, keeping the 10 mM electrolyte concentration ( $\hat{\lambda}_D$ = 3.03) constant, while varying the channel heights $\hat{L}_y$. The particle travels in a confined region, which becomes greater with increasing channel height, while the EDL thickness (scaled with particle radius) remains the same. Therefore, $\hat{\lambda}_D$ and $\hat{L}_y$ can be used to estimate the confined region. When the EDL from the particle overlaps the EDL from the wall, there is a repulsive force on the particle. We use $3\hat{\lambda}_D$ as a characteristic value of the EDL thickness, because it represents the point when the electric potential drops to ~5% of the surface value, when considering linearized Debye-Huckel theory [55]. Therefore the confined region can be estimated by $\hat{h}_{05} = \hat{L}_y - 4 \times \left(3\hat{\lambda}_D\right)$ when the particle size is insignificant compared to the channel height. The estimated confined regions $\hat{h}_{05}$ are shown in Figure 4.5 as the dashed lines. The results indicate that $\hat{h}_{05}$ is a good estimation, although it overpredicts the confined region for all cases (from 4% to 29%).

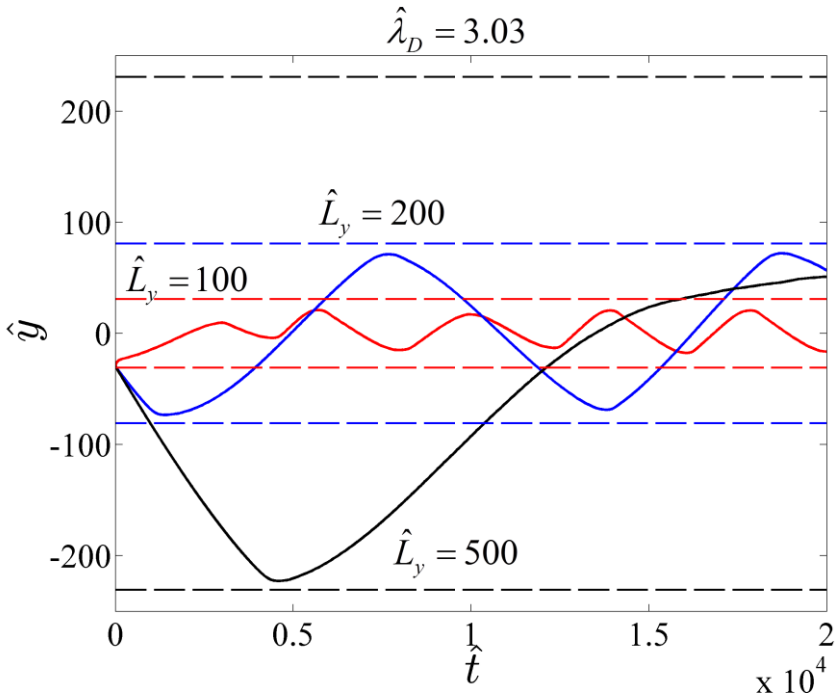


Figure 4.5. Particle transverse location as a function of time with 10 mM electrolyte concentration ( $\hat{\lambda}_D$ = 3.03) in channels with different heights $\hat{L}_y$ = 100, 200, and 500. The particle moves in an oscillatory manner in a confined region. The confined region increases as the channel height increases, and it can be estimated by $\hat{h}_{05} = \hat{L}_y - 12\hat{\lambda}_D$ (dashed lines).

Next, we investigate the oscillatory movement of the particle in more detail. Due to symmetry, we only consider the particle in the lower half of the channel. Since thermal fluctuations are excluded in our simulations, the oscillatory particle motion in a 10 mM electrolyte solution is caused by the electric force and fluid stress on the particle. Figure 4.6 shows the net transverse force and moment on the particle as a function of the particle angle at 4 different locations. Here we used the approaches from the steady-state model to calculate the force and moment.[16] When the particle is at the centerline ( $\hat{y}_p = 0$ ) or near the centerline ( $\hat{y}_p = -10$ ), the moment on the particle is relatively small and can be neglected, and the net transverse force depends only on the angle of the particle. This indicates that

translation dominates the particle motion in this region, and the particle translates towards the wall, if $0° < \theta < 90°$ due to the negative transverse force.

When the particle is at $\hat{y}_p = -20$, near the lower confinement boundary $\hat{y} \approx -21$ (see Figure 4.3), the transverse force becomes more positive for all angles as shown in Figure 4.6(a), which is due to the repulsive force from the bottom wall. In addition, the moment on the particle is significant (as shown in Figure 4.6(b)) and it changes with the angle of the particle. Two zero moment points can be observed at $\theta = 86°$ and $\theta = -12°$, which results from the flow stress and the electric force on the particle. The slope of the moment-angle line indicates only $\theta = -12°$ is a stable equilibrium point. If the particle is located outside the confined region ($\hat{y}_p = -25$), the repulsive force dominates and the net transverse force becomes positive for all angles. Therefore the particle will move quickly into the confined region regardless of its orientation.

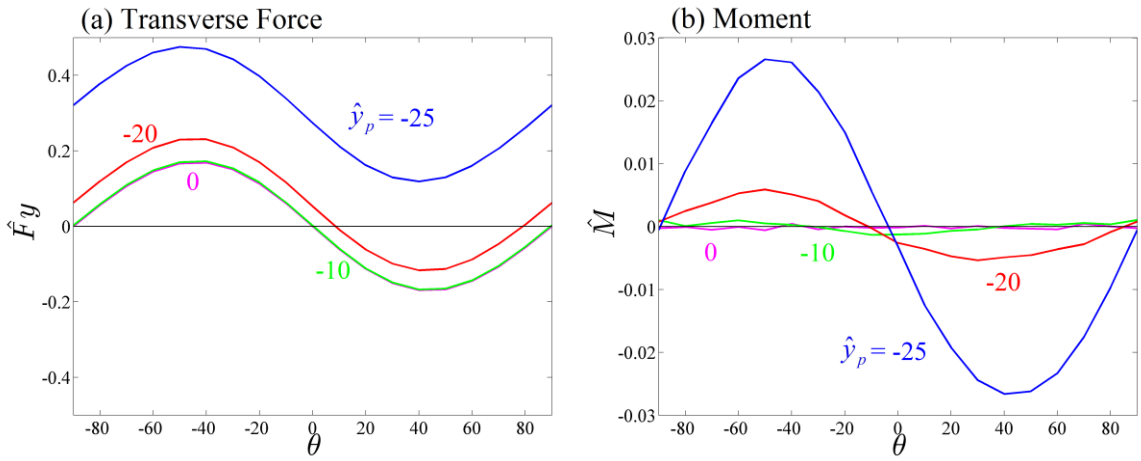


Figure 4.6. Transverse force and moment on the particle as a function of particle angle in a 10 mM electrolyte solution. The transverse force becomes positive everywhere when the particle is outside the confined region ($\hat{y}_p = -25$). The moment is small when the particle is near the centerline of the channel.

The particle tends to keep its angle at the stable equilibrium angle ($\theta_{stable} = \pm 12°$ near the top and bottom boundaries of the confined region), due to the net moment on the particle. Figure 4.7 shows the angle of the particle as a function of time for 10 mM electrolyte concentration ($\hat{\lambda}_D$ = 3.03). The observed angle in a 100 nm channel ($\hat{L}_y$ = 100, solid line) is bounded by $\theta_{bound} = \pm 14°$, which agrees well with the stable equilibrium angle. Angle confinement can be observed in a larger channel ($\hat{L}_y$ = 200, dashed line) with similar bounds. This indicates nanochannels confine both the transverse location and angle of the particle. Note that the stable equilibrium angle may change with both the electrolyte concentration and the particle location.

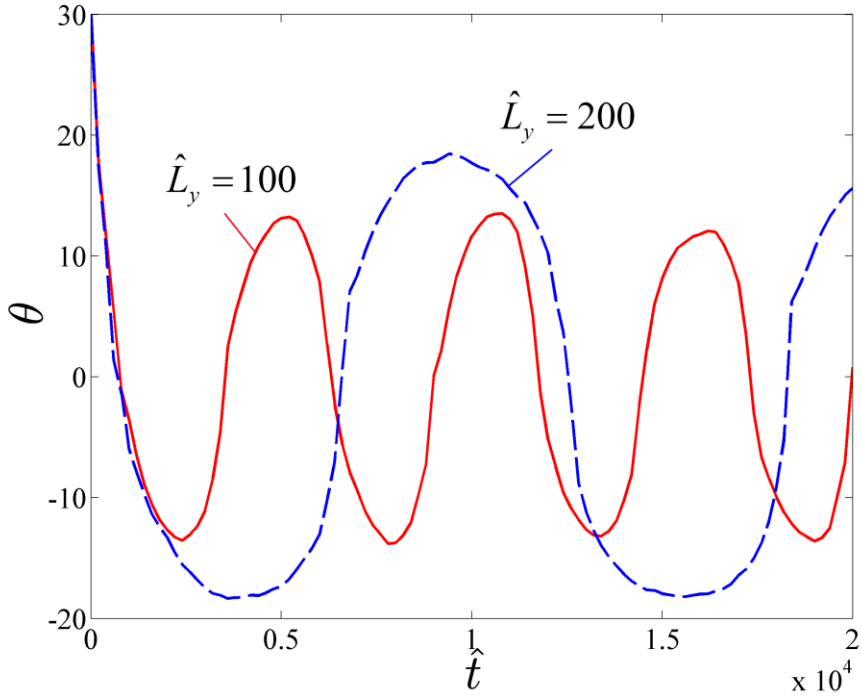


Figure 4.7. The angle (in degree) of the particle as a function of time in a 10 mM electrolyte solution ( $\hat{\lambda}_D$ = 3.03) for $\hat{L}_y$ = 100 (solid line) and $\hat{L}_y$ = 200 (dashed line). The angle observed for $\hat{L}_y$ = 100 is bounded by $\theta = \pm 14°$, which is close to the stable equilibrium angle estimated by calculating moment on the particle. Similar angle confinement can also be observed in a larger channel.

Thermal fluctuations are neglected in the current numerical simulations. However, the effect of thermal fluctuations can be estimated from the particle Péclet number $Pe_p = UL/D_p$, where $U$ is the characteristic velocity, $L$ is the characteristic length, and $D_p \approx k_B T / 6\pi\eta a$ is the particle diffusion coefficient. Here we approximate $L$ ~ 100 μm, since the order of particle velocity is ~10 μm/s and the time for measuring average particle velocity in experiments is ~10 s. For 10 mM electrolyte concentration, we have $Pe_{p,x} \approx 0.54$ in *x-direction*, indicating that motion due to thermal fluctuations are on the same order as the electrophoretic-induced motion. However when the average mobility measured over a

significantly longer time period, it should not be affected by thermal fluctuations. Therefore, the mobility estimates from the deterministic numerical simulations should be reasonably accurate. In comparison, the velocity in *y-direction* is about 2% of that in the *x* direction, which results in a significantly smaller Péclet number $Pe_{p,y} < 0.01$ for the *y-direction*. This indicates that diffusion in *y-direction* dominates, and the smooth oscillatory motion of the particle may not be observed in practical cases. Nevertheless, the confinement should still present due to the strong repulsive forces from the wall EDLs.

### 4.2.2. Particle Mobility

From the previous section, the particle's transverse location was found to be dominated by the EDL thickness, which is dependent directly upon the electrolyte concentration. In addition, the particle mobility changes for different transverse locations. Therefore, the overall particle mobility also depends upon the distribution of transverse particle location. The distribution of transverse particle location can be estimated by tracking the particle location as a function of time. For example, the particle transverse location from Figure 4.3 is sampled at each non-dimensional time step to construct the histograms shown in Figure 4.8. Due to symmetry, we report one-sided histograms of particle location. The estimated confined regions $\hat{h}_{05}$ from the previous section are plotted as the dashed lines for both cases. Since the double layers overlap significantly for the 1 mM case ($\hat{h}_{05} < 0$), the boundary of the confined region is plotted at $\hat{y} = 0$. This indicates that the particle should always be confined to the centerline, as observed from the distribution, and as concluded from the previous section. For the 10 mM case, the distribution is bounded by $\hat{h}_{05}$, and several peaks

on the histogram are observed near the boundary of the confined region. The increased repulsive force reduces the particle transverse velocity when it is located near the boundary. With the lower speed, the particle tends to stay longer near the boundary of the confined region, and therefore the particle can be observed with higher probability, which agrees with the classical probability distribution, $P(y) \sim 1/u_y(y)$.

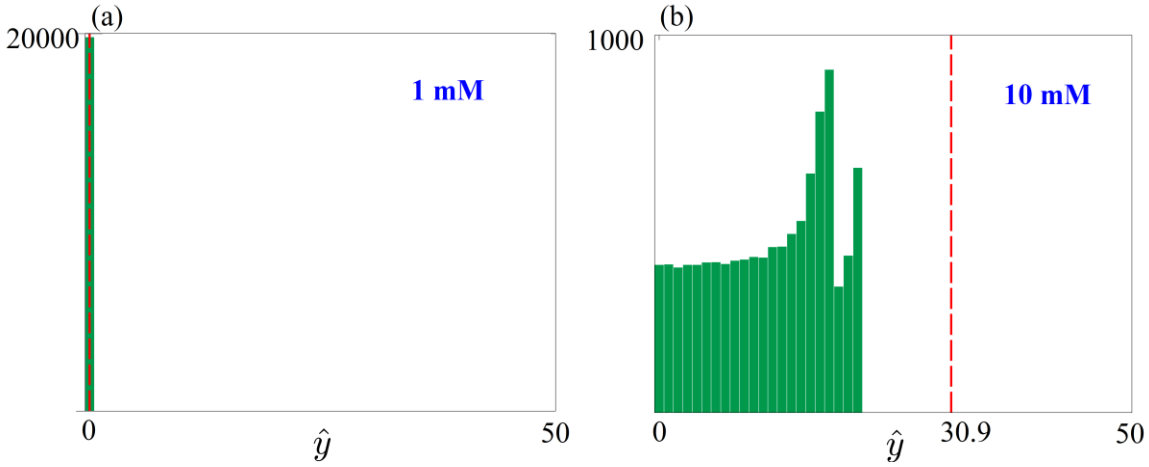


Figure 4.8. Particle distribution as a function of the particle location from the centerline to the side wall for (a) 1 mM and (b) 10 mM electrolyte concentration. The estimated confined regions $\hat{h}_{05}$ are also plotted as the dashed lines. For 1 mM the particle is subject to the repulsive force, even with slight deviation and therefore it is confined to the centerline. For 10 mM, the EDL screening is stronger and the particle does not sense the repulsive force until it is close to the boundary of the confined region, which explains the wider distribution.

To obtain a comprehensive understanding of the confinement effect, we plot several particle distributions along with the estimated confined region in Figure 4.9. Here we consider 1, 10, 20, 50 mM electrolyte concentrations, and three different particle geometries: 2 nm × 3.4 nm, 2 nm × 6.8 nm, and 2 nm × 17 nm. The distribution becomes wider with increased electrolyte concentration due to reduced EDL thickness and stronger screening.

Particle size does not affect significantly the location distribution, compared to electrolyte concentration. It is important to note that our simulations exclude thermal fluctuations, which would most likely modify the distribution of the particle in reality.

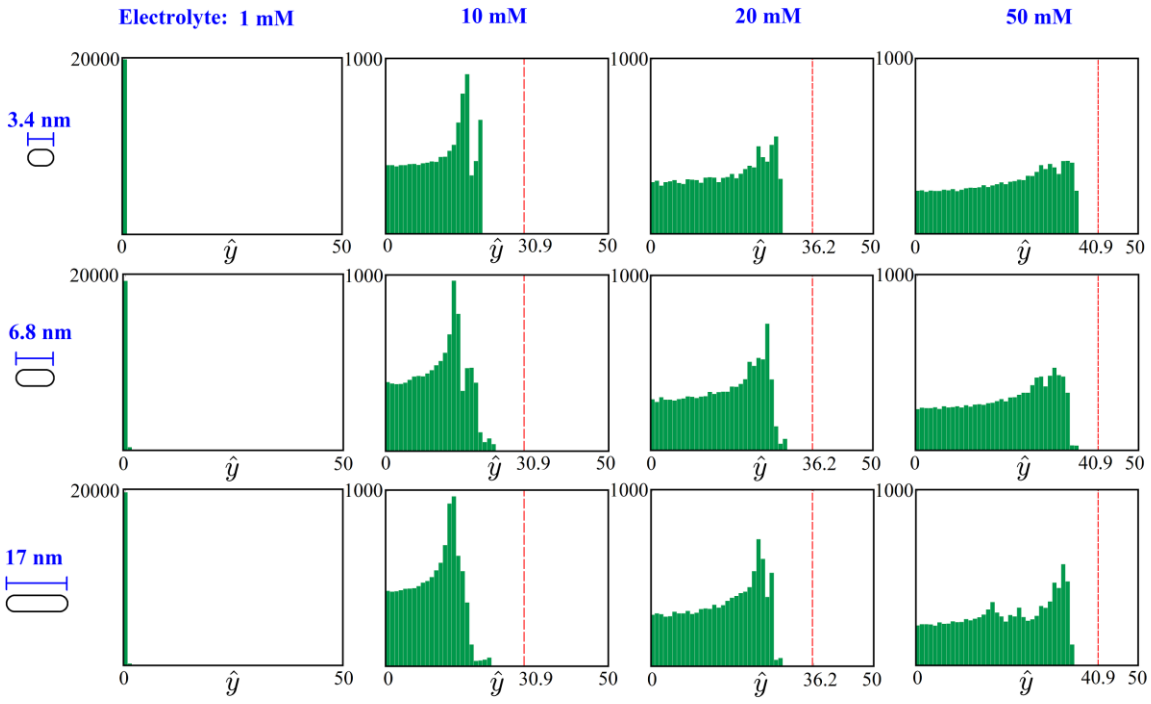


Figure 4.9. Particle distribution as a function of the particle location from the centerline to the side wall for different electrolyte concentrations and particle geometries. The distribution becomes wider with increased electrolyte concentration due to reduced EDL thickness. The estimated confined regions are also shown as the dashed lines.

The average mobility of the particle from the deterministic numerical simulation is calculated by dividing the total displacement by time. In addition, the approximate mobility can be obtained using the steady-state model from our previous work. Figure 4.10 shows dimensionless electrophoretic mobility from the two models (circles for the steady-state model and squares for the current deterministic numerical simulation model) as a function of electrolyte concentration for three different particle geometries. For low concentrations, the

mobility from the two models are in good agreement, because the particle is confined at the centerline. As concentration increases, the confinement gets weaker and the mobility is overpredicted (~10% higher) by the steady-state model. Since the particle translates and rotates simultaneously, the inclination of the particle increases the hydrodynamic drag and thus reduces particle mobility. Interestingly, particle geometry has greater influence on particle mobility than EDL confinement. Mobility is higher for higher aspect-ratio particles, because higher total electrical charge results in larger electric forces and higher velocities. In summary, the confinement is dominated by EDL thickness through electrolyte concentration, while the mobility can be affected by particle geometry due to the surface charge. The deterministic numerical simulation is required to calculate mobility accurately as electrolyte concentration is higher than 50 mM.

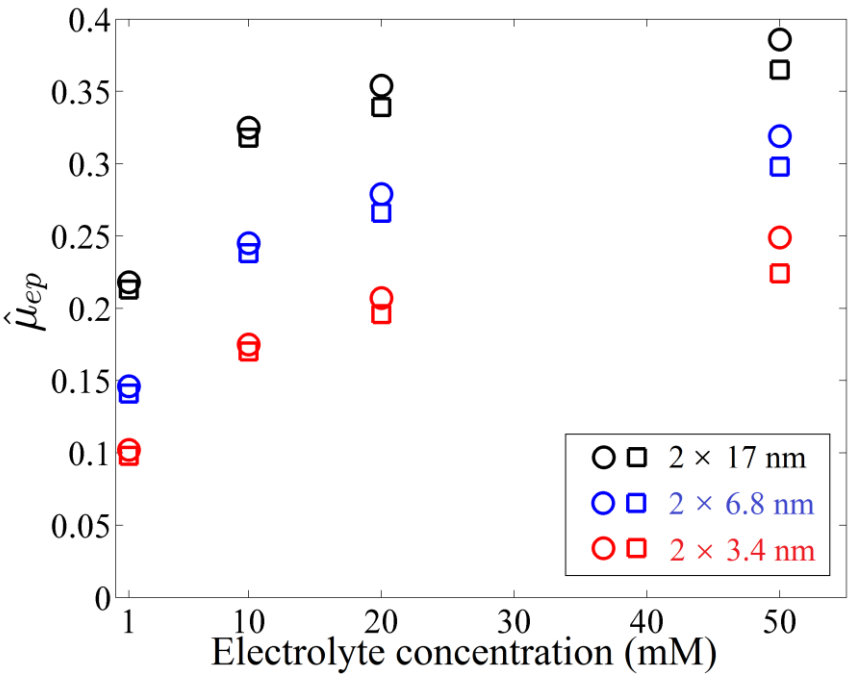


Figure 4.10. Electrophoretic mobility as a function of electrolyte concentration. The circles and squares correspond to steady-state model and the deterministic numerical simulation, respectively. The mobility from steady-state model is 10% higher than that calculated by deterministic simulation for 50 mM electrolyte concentration.

# 5. Zeta Potential Estimation

In this chapter we use our model to estimate zeta potential of particles by the measured mobility from experiments. We focus on spherical particles and examine the effects of thermal fluctuations and particle migration. The double layer polarization and double layer interaction will both affect the zeta potential estimation, and the importance of electrolyte composition is also investigated.

## *5.1. Thermal Fluctuations*

The importance of thermal fluctuations can be estimated from the particle Péclet number $Pe_p = UL/D_p$, where $U$ is the characteristic velocity, $L$ is the characteristic length, and $D_p \approx k_B T/6\pi\eta a$ is the particle diffusion coefficient. Here we approximate $L$ ~ 1 mm, since the order of particle velocity is ~100 μm/s and the time for measuring average particle velocity in experiments is ~10 s. For a 42 nm-diameter particle, we have $Pe_{p,x} \approx 9.79\times10^3$, indicating that motion due to thermal fluctuations is insignificant compared to electrophoretic-induced motion. The particle diffusion coefficient will further decrease if the size of particles increases, which results in even higher value of particle Péclet number. Therefore, the mobility estimates from the deterministic numerical simulations should be reasonably accurate.

## *5.2. Particle Migration*

To evaluate the influence of particle migration, we compare the mobility of the particle in the steady-state model and the fluid-structure interaction model. The 42 nm-diameter

particle in a 100 nm-height channel was investigated. The zeta potentials of the particle and the walls were taken as -1 mV and -2 mV, respectively. Figure 5.1 shows trajectory of the particle initially located near lower wall of the channel with 1 mM electrolyte concentration. The repulsive forces from the walls keep the particle moving near the center plane.

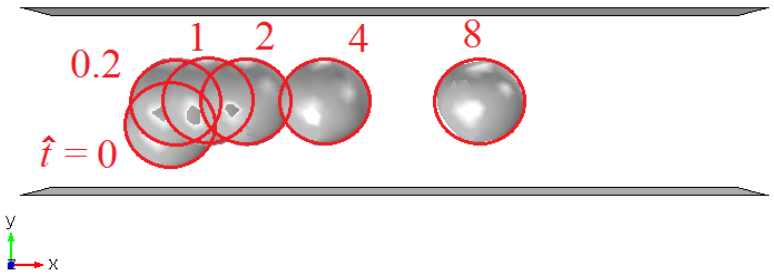


Figure 5.1. Trajectory of a 42 nm-diameter particle in a 100 nm-height channel with 1 mM electrolyte concentration. The zeta potentials of the particle and the walls were -1 mV and -2 mV, respectively. The repulsive forces on the particle keep it moving along the center plane. The average mobility is calculated by the total travel distance and the time required.

The dimensionless total mobility is calculated by the total travel distance and the time used, and the results are shown in Table 5.1, along with the mobility calculated from the steady-state model. A good agreement between the two models indicate that the steady-state model is a good approximation to study electrophoresis of a 42 nm spherical particle. Because of the symmetric geometry of the particle, the drag difference from the orientation (with respect to the flow direction) is insignificant. Therefore the steady-state model is used to study electrophoretic motion of spherical particles and to estimate particle zeta potential.

| Electrolyte concentration (mM) | Total mobility, steady-state model ($10^{-10}m^2/Vs$ ) | Total mobility, fluid-structure interaction model ($10^{-10}m^2/Vs$ ) |
|---|---|---|
| 1 | 8.98 | 9.17 |
| 10 | 8.29 | 7.95 |

Table 5.1. Mobility in steady-state model and fluid-structure interaction model. Here we consider a 42 nm particle in a 100 nm channel. Two electrolyte concentrations (1, 10 mM) are used here, and a good agreement between the two models can be observed.

### *5.3. Particle Zeta Potential Calculation*

5.3.1. Wynne et al. 2012 [38]

In this paper the total mobility of 42 nm-diameter particle in 100-nm height channel was measured. Sodium-borate buffer solutions of pH 9 with 5, 10, 50 mM concentration are used as electrolyte solution. The wall zeta potential was measured by current monitoring. Table 5.2 shows the particle zeta potentials predicted by our steady-state model. Here we also list the zeta potentials calculated by classic models (Smoluchowski and Huckel), and those values can be used as the lower and upper bounds.

| Electrolyte concentration (mM) | Total mobility ($10^{-8}\,m^2/Vs$) | Wall zeta potential (mV) | Particle zeta potential (mV) | Smoluchowski $\mu = \frac{\varepsilon\zeta_p}{\eta}$ (mV) | Huckel $\mu = \frac{2}{3}\frac{\varepsilon\zeta_p}{\eta}$ (mV) |
|---|---|---|---|---|---|
| 1 | 5.86 | -115 | -46.1 | -24.9 | -37.3 |
| 10 | 4.67 | -101 | -48.9 | -30.6 | -45.9 |
| 50 | 2.19 | -80.1 | -66.4 | -51.3 | -77.0 |

Table 5.2. Particle zeta potential from measured total mobility and wall zeta potential. The particle is 50 nm and the channel height is 100 nm. Three different electrolyte concentrations are considered with pH = 9. Here we also listed the zeta potentials calculated from Smoluchowski and Huckel's expressions as references.

For low electrolyte concentrations (1, 10 mM) the particle zeta potentials predicted by our model are not bounded by the values from classic models. This may be due to double layer polarization (the nonlinear effect) and the interaction of the EDLs of the particle and walls. For the thick EDL (1 mM case) the predicted zeta potential is much greater than the ones from the classic models. Since the zeta potentials are not very high compared to thermal potential ($\zeta e / k_B T < 2$), the interaction of EDLs would be the major reason for the discrepancy. The results show that our model is required to find the correct value of zeta potential with double layer interaction.

5.3.2. Napoli et al. 2011 [39]

In this paper wall zeta potentials were estimated by Smoluchowski's formula, which used measured velocity of fluorescein in the channel and the charge of the fluorescein. Then

the electrophoretic mobility was obtained by the measured particle velocity and the wall zeta potentials. Electrophoretic mobility of 50 and 100 nm-diameter particle in 100 nm, 1 um, and 20 um-height channel are shown in Table 5.3. Acetate (pH 5), phosphate (pH 7), and borate (pH 9) with 1 and 10 mM concentration were used as electrolyte solutions. Here we also list the zeta potentials calculated by classic models (Smoluchowski and Huckel) as reference.

| Particle diameter | Channel height | pH | Electrolyte concentration (mM) | Electrophoretic mobility ($10^{-8}$ $m^2$/Vs ) | Particle zeta potential (mV) | Classic models (mV) |
|---|---|---|---|---|---|---|
| 50 nm | 250 nm | 5 | 1 mM | -1.44 | -30.0 | (-20.3, -30.4) |
| | | | 10 mM | -0.032 | -0.57 | (-0.46, -0.69) |
| | | 7 | 1 mM | -1.28 | -26.9 | (-18.3, -27.5) |
| | | | 10 mM | -2.34 | -45.4 | (-33.5, -50.2) |
| | | 9 | 1 mM | -5.20 | NA | (-72.5, -109) |
| | | | 10 mM | -2.90 | -59.3 | (-41.5, -62.2) |
| | 1 μm | 5 | 1 mM | -1.29 | -26.9 | (-18.5, -27.7) |
| | | | 10 mM | 0.346 | 6.30 | (4.95, 7.42) |
| | | 7 | 1 mM | -2.81 | -67.6 | (-40.1, -60.2) |
| | | | 10 mM | -2.62 | -52.2 | (-37.5, -56.2) |
| | | 9 | 1 mM | -9.51 | NA | (-136, -204) |
| | | | 10 mM | -4.39 | NA | (-62.8, -94.1) |

| | | | | | | |
|---|---|---|---|---|---|---|
| | 20 μm | 5 | 1 mM | -2.04 | -44.7 | (-29.1, -43.7) |
| | | | 10 mM | -1.43 | -26.3 | (-20.4, -30.7) |
| | | 7 | 1 mM | -3.24 | -86.2 | (-46.3, -69.5) |
| | | | 10 mM | -2.16 | -41.2 | (-30.9, -46.3) |
| | | 9 | 1 mM | -7.80 | NA | (-112, -167) |
| | | | 10 mM | -3.80 | -97.0 | (-54.3, -81.5) |
| 100 nm | 250 nm | 5 | 1 mM | -1.83 | -37.7 | (-26.1, -39.2) |
| | | | 10 mM | -1.87 | -32.5 | (-26.7, -40.1) |
| | | 7 | 1 mM | -1.90 | -39.4 | (-27.2, -40.8) |
| | | | 10 mM | -4.03 | -84.6 | (-57.6, -86.4) |
| | | 9 | 1 mM | -5.13 | NA | (-73.4, -110) |
| | | | 10 mM | -3.04 | -56.1 | (-43.5, -65.2) |
| | 1 μm | 5 | 1 mM | -3.24 | -77.8 | (-46.3, -69.5) |
| | | | 10 mM | -0.984 | -16.4 | (-14.1, -21.1) |
| | | 7 | 1 mM | -3.92 | NA | (-56.0, -84.0) |
| | | | 10 mM | -4.04 | -81.4 | (-57.8, -86.7) |
| | | 9 | 1 mM | -9.67 | NA | (-138, -207) |
| | | | 10 mM | -5.45 | NA | (-77.9, -117) |
| | 20 μm | 5 | 1 mM | -3.22 | -76.9 | (-46.0, -69.0) |
| | | | 10 mM | -2.72 | -48.6 | (-38.9, -58.3) |
| | | 7 | 1 mM | -4.26 | NA | (-60.9, -91.4) |
| | | | 10 mM | -4.28 | -91.3 | (-61.2, -91.8) |
| | | 9 | 1 mM | -10.2 | NA | (-146, -219) |

| | | | | | | |
|---|---|---|---|---|---|---|
| | | | 10 mM | -4.66 | NA | (-66.6, -99.9) |

Table 5.3. Particle zeta potential from measured electrophoretic mobility. Two particles (50 and 100 nm) and three channel heights (250 nm, 1 μm, 20 μm) are considered, and three electrolyte solutions (pH = 5, 7, 9) are used with two concentrations (1, 10 mM). Here we also listed the zeta potentials calculated from Smoluchowski and Huckel's expressions as references.

We notice that there 6 predicted zeta potentials locating outside the region by classic models. The channel height is large compared to the particle size and Debye length. Therefore the discrepancy should come from double layer polarization. In addition, no proper zeta potentials can be determined in 11 cases, because the measured mobility is greater the maximum value predicted by the model. As we discussed in chapter 3, the electrophoretic mobility first increases with zeta potential and then decreases due to the double layer polarization, which results in a maximum mobility for a given electrolyte concentration.

We plot the mobility as a function of zeta potential in Figure 5.2. Here we used a 50 nm-diameter particle in a 2 μm-height channel. The channel height is relatively large compared to the particle so the boundary effect is minimized. We find the maximum mobility are $-3.76\times10^{-8}$ and $-3.95\times10^{-8}$ $m^2/Vs$ for 1 and 10 mM electrolyte concentration, respectively. Similarly we obtained the maximum mobility for 100 nm-diameter particle in a 2 μm-height channel. The maximum mobility for 100 nm particle are $-3.71\times10^{-8}$ and $-4.61\times10^{-8}$ $m^2/Vs$ for 1 and 10 mM electrolyte concentration, respectively. Therefore we cannot obtain zeta potential for the 11 cases with electrophoretic mobility greater than the maximum value.

A possible explanation is that the buffer solutions in the experiments are not a simple (+1, -1) electrolyte solution. The negative ions may be a combination of ions with different valences. Here we consider a simple case with (+1, -2) electrolyte solution with the same ionic strength. Then we follow the similar approach to calculate the mobility for 50 nm-diameter particle in 20 μm-height channel as in Figure 5.2. The new maximum mobilities are $-4.14\times10^{-8}$ and $-5.02\times10^{-8}$ $m^2/Vs$ (11.6% and 8.89% increase) for 1 and 10 mM ionic strength, respectively. This indicates the composition of electrolyte solution is also important to determine the particle zeta potential.

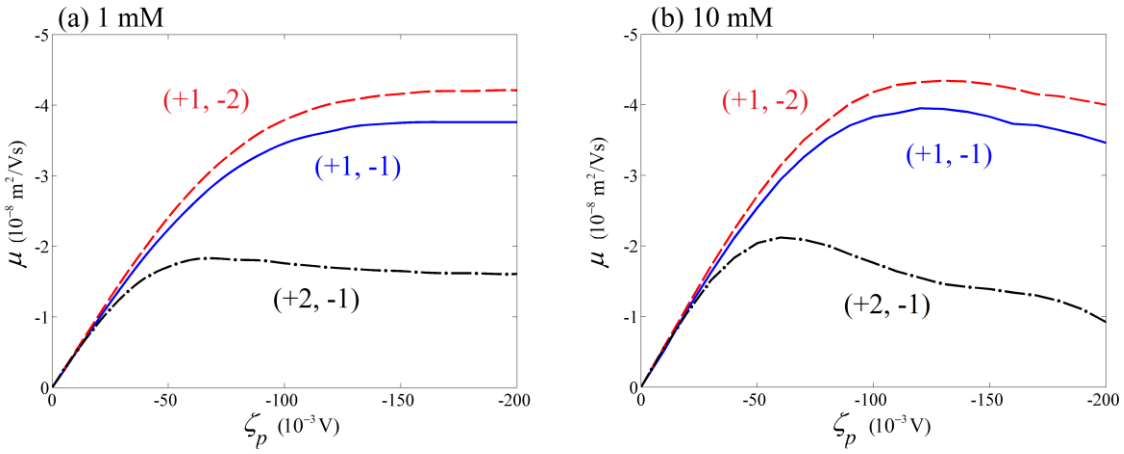


Figure 5.2. Mobility as a function of particle zeta potential of 50 nm particle in 20 μm channel in electrolyte solutions with (a) 1 mM and (b) 10 mM ionic strength. Solid, dashed and dashed-dotted lines correspond to electrolyte with valences (+1, -1), (+1, -2), (+2, -1), respectively.

We also plotted the mobility as a function of zeta potential in (+2, -1) electrolyte solutions in Figure 5.2. The results show that the maximum mobility decreases drastically compared to (+1, 1) electrolyte, and the location of the maximum shifts to lower zeta potentials. In this case the particle is negatively charged, and the positive ions are attracted

near it to form EDL. When the valence of positive ions increases, the electric force on the fluid near the particle increases. Therefore the drag force on the particle increases and results in the lower mobility.

5.3.3. Semenov et al. 2013 [56]

In this paper they measured amplitude and phase of the oscillatory particles under AC electric field in a symmetric micro fluidic cell by using optical tweezers. The particle diameter is 2.23 μm and the channel is 0.3 mm × 1 mm in cross-section. Three different electrolyte (KCl, $CaCl_2$, $LaCl_3$) with different concentrations (or ionic strength) were used in the experiments. Table 5.4 shows the results of particle zeta potentials predicted by our model and by the classic models. Since the channel height is much greater than the particle, EDLs will not interact with each other. Therefore the case locating outside the classic region is caused by double layer polarization. In addition, positive mobilities were observed in three cases for $LaCl_3$ electrolyte solution, and the predicted zeta potentials are not bounded by the values from classic models. Since the zeta potentials are not high enough to cause double layer polarization, it indicates that the classic models may not be directly applied to trivalent electrolyte with charge inversion. For $CaCl_2$ and $LaCl_3$ at 10 μM concentration, our model cannot provide a valid zeta potentials because the measured mobilities are greater than the maximum mobility. One possible reason is that the concentration of the proton (1.58 μM for a pH=5.8 solution) is comparable to the positive ions. Therefore the concentration of positive ions would be greater than 10 μM, and the valence and diffusion coefficient of the ions are not constants, which can affect the particle mobility measured in experiments.

| Electrolyte | Electrolyte concentration (mM) | Electrophoretic mobility ($10^{-8}\,m^2/Vs$) | Particle zeta potential (mV) | Classic models (mV) |
|---|---|---|---|---|
| KCl | 400 | -1.33 | -19.1 | (-19.0, -28.5) |
| | 100 | -1.45 | -21.1 | (-20.7, -31.1) |
| | 10 | -2.36 | -35.9 | (-33.7, -50.6) |
| | 1 | -3.28 | -51.1 | (-46.9, -70.3) |
| | 0.4 | -4.37 | -70.2 | (-62.5, -93.7) |
| | 0.1 | -4.75 | -88.9 | (-67.9, -102) |
| | 0.04 | -4.21 | -83.7 | (-60.2, -90.3) |
| | 0.01 | -3.55 | -78.8 | (-50.8,-76.1) |
| $CaCl_2$ | 100 | -0.578 | -9.50 | (-8.26, -12.4) |
| | 10 | -1.09 | -17.3 | (-15.6, -23.4) |
| | 1 | -1.64 | -23.9 | (-23.4, -35.2) |
| | 0.1 | -2.54 | -42.5 | (-36.3, -54.5) |
| | 0.01 | -3.34 | NA | (-47.7, -71.6) |
| $LaCl_3$ | 100 | 0.707 | 8.10 | (10.1, 15.2) |
| | 40 | 0.610 | 7.78 | (8.72, 13.1) |
| | 10 | 0.369 | 5.24 | (5.28, 7.91) |
| | 4 | 0 | 0 | (0, 0) |
| | 1 | -0.514 | -8.76 | (-7.35, -11.0) |
| | 0.4 | -0.916 | -13.6 | (-13.1, -19.6) |

| | | | | |
|---|---|---|---|---|
| | 0.1 | -1.46 | -22.5 | (-20.9, -31.3) |
| | 0.01 | -2.3 | NA | (-32.9, -49.3) |

Table 5.4. Particle zeta potential from measured electrophoretic mobility. A 2.23 μm particle is used in a large channel (0.3 mm × 1 mm), and three electrolyte (KCl, $CaCl_2$, $LaCl_3$) are used with several concentrations. Here we also listed the zeta potentials calculated from Smoluchowski and Huckel's expressions as references.

The results show that our model can be used to obtain accurate zeta potentials of the particles, while the classic models fail to capture double layer polarization and double layer interaction.

# 6. Conclusions and Future Directions

## *6.1. Conclusions*

Numerical simulation was used to investigate the electrophoretic mobility of a spherical particle in a confined nanochannel. The numerical model was validated for a wide range of zeta potentials, electrolyte concentrations, and channel sizes. The results indicate that, for a 50 nm spherical nanoparticle in a 100 nm nanocahnnel, the mobility of a particle located at the centerline of the nanochannel agrees to within 1% of the average mobility for a particle distributed transversely throughout the nanochannel.

When a nanoparticle is confined in a nanochannel, overlapping EDLs between the charged particles and nanochannels walls can be important. Charged walls not only induce a background flow (electro-osmotic flow), but also affect the particle's hydrodynamic drag and surface charge density. Particle mobility in nanochannels can be greater than that in microchannels, if the electrolyte concentration is chosen properly.

The numerically-simulated results indicate that different size nanoparticles may be electrophoretically-separated using nanochannels, even if the particles have similar zeta potentials. For example, a 100 nm-wide nanochannel could be used to separate 50 nm and 10 nm-diameter particles for a wide range of electrolyte concentrations. A new method is proposed for determining zeta potentials of the particle and channel walls by measuring the mobility of a particle using two different height channels. This method can avoid errors generated from measuring electro-osmotic velocity, and it is applicable over a wide range of zeta potentials.

Next, fluid-structure interaction is included in the model to investigate particle mobility and the confinement effect of a two-dimensional rod-like particle in a nanochannel. The results indicate that different particle motions can be observed in electrolyte solutions with different concentrations. For the 1 mM case, the particle is confined at the centerline of the channel due to the overlapping EDLs between the charged particles and nanochannels walls. When electrolyte concentration is increased, the particle can move in a confined region, which is roughly predicted by the estimated confined region $\hat{h}_{05}$. The confined region is determined by the electrolyte concentration as well as the channel height. In addition, the oscillatory particle motion can be explained by examining the transverse force and the moment on the particle, which show a strong dependence on the angle and the transverse location of the particle. Due to the interactions of the EDLs from the wall and the particle, stable equilibrium angles of the particle exist and the observed angle during the motion lies mostly within the stable equilibrium angle at the boundary of the confined region.

The distribution of transverse particle location within the confined region is important because it affects the overall particle mobility. Simulations were conducted to study the distribution using three different sizes of rod-like particles and four different electrolyte concentrations, in a 100 nm high nanochannel.

Particle mobility was calculated using the deterministic numerical simulation model, and compared to the approximate particle mobility obtained from our previously reported steady-state model. The results agree well for the 1 mM electrolyte case. However, for the 50 mM case, the calculated mobilities differ by up to 10 %. This indicates the importance of using the deterministic numerical simulation model to obtain accurate non-spherical particle mobility when considering high electrolyte concentrations.

Finally, we combine our model with the experimental data to estimate particle zeta potential. The effects of electromigration and thermal fluctuations are insignificant when we consider spherical particle with diameter greater than 42 nm under moderate external electric field. The results show that the classic models fail to provide accurate zeta potential because double layer polarization and interaction affect particle mobility for higher zeta potential in a narrow channel. In addition, the composition of electrolyte solution also affects the particle mobility. Therefore it is also important to understand the properties of electrolyte solutions in each experiment.

### *6.2. Future Directions*

In this work we mostly studied electromigration of 2D rods due to the computational limits. Here we show some preliminary results for motion of a 3D rod in a channel. Figure 6.1 shows the trajectory of a nanorod with 2 nm-diameter and 3.4 nm-height in a 100 nm-height nanochannel in a 1 mM KCl solution. The applied external electric field is 1000 V/m, and the zeta potentials of the particle and the walls are -1 mV and -2 mV, respectively. Due to the interaction of the thick EDLs, the particle moves toward the center plane and stay near it, which is similar to the motion of 2D rods for lower electrolyte concentrations in chapter 4. However, the major axis of the rod does not align with the direction of the flow. This is because the 3D rod is able to move in *z-direction* and rotate about *y-axis*, which are not allowed in 2D simulations. Since the hydrodynamic force on the particle is affected by the angle between the rod and flow direction, the velocity of a 3D nanorod changes with its location and orientation in an unsteady manner. Therefore, the steady-state model with assumption of an aligned rod in a channel cannot provide an accurate mobility.

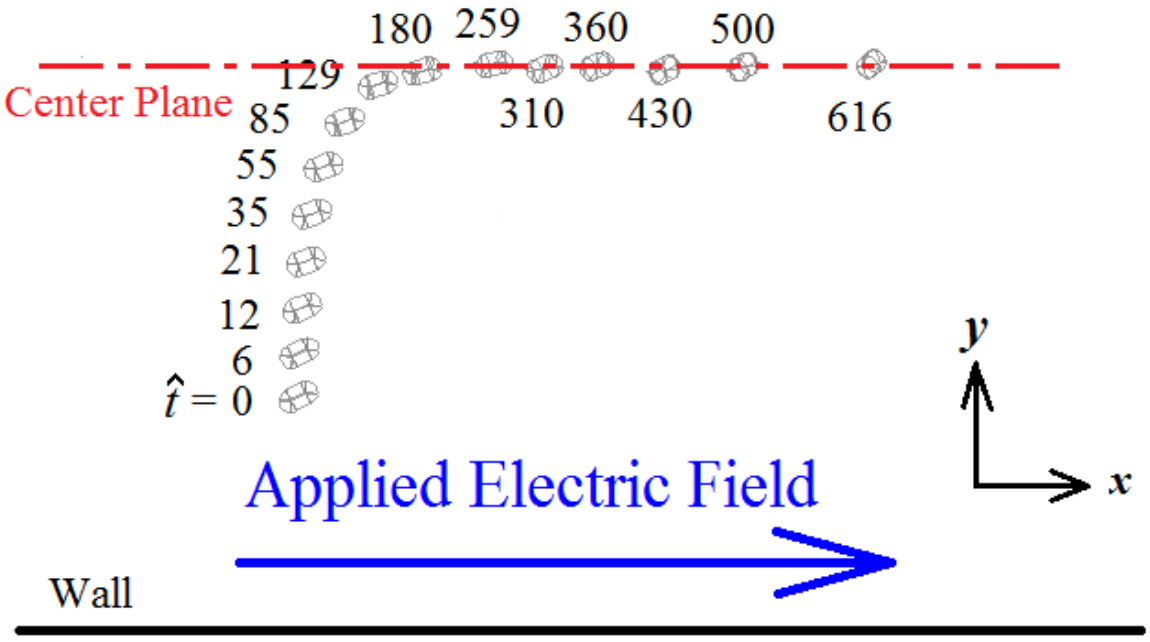


Figure 6.1. Trajectory of a nanorod in a nanochannel with 1 mM KCl electrolyte solution. The repulsive forces from the wall make the particle move toward the center plane. The major axis of the rod does not align with the direction of applied electric field because the rod can rotate about *y-axis*. The velocity of the particle changes with its location as well as orientation so only averaged mobility can be obtained.

Figure 6.2 shows the trajectory of the same nanorod in a 20 mM KCl solution. Since the EDLs are thinner, the repulsive forces on the particle reduce to zero before it reaches the center plane. The rotation of the rod is stronger compared to 1 mM case, so the drag force changes rapidly as well as the velocity.

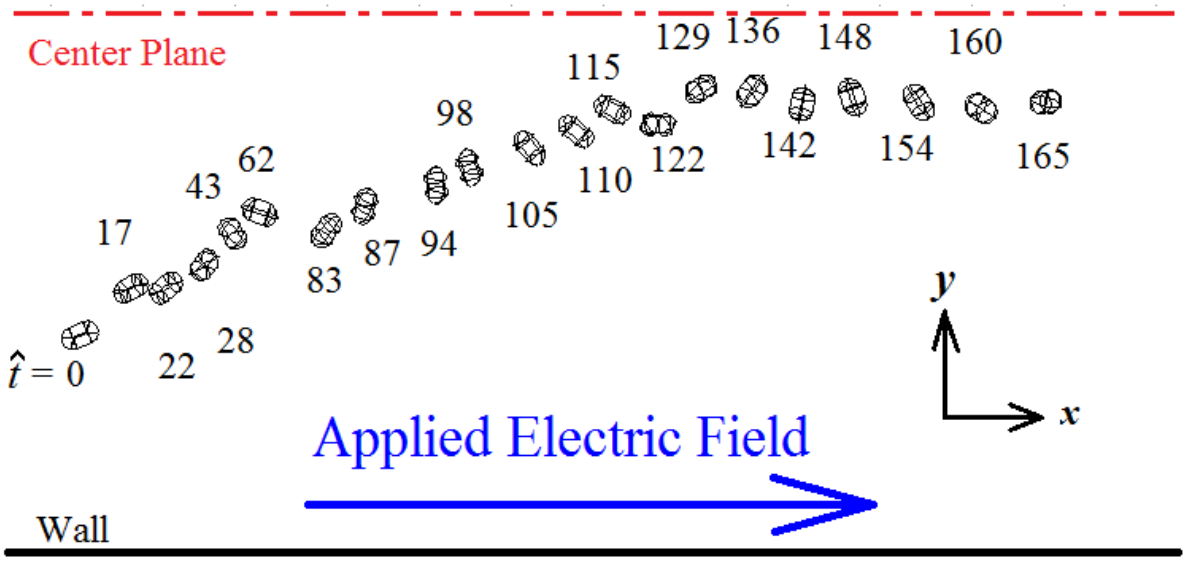


Figure 6.2. Trajectory of a nanorod in a nanochannel with 10 mM KCl electrolyte solution. The particle still moves toward the center plane but it does not reach it due to thinner EDLs. The rotation of the particle is much stronger than 1 mM case, and the variation of orientation affects its velocity and the average mobility.

The above preliminary results show that the steady-state assumption is not valid for a rod-like particle. Therefore a comprehensive model including fluid-structure in a 3D domain is required to calculate the accurate mobility. However, the 3D fluid-structure simulations require a great number of meshes to capture the sharp change inside the EDLs, so it requires better hardware and takes longer time to find a solution. High speed computing such as parallel computing could be a solution to improve the efficiency of computation. In addition, since the system of equations are highly coupled, the convergence of the simulation is also an issue. An improvement of the solver is helpful to reduce iteration time and to make the simulation more stable.

Although thermal fluctuations may not be important for large particles, they could be important when we consider smaller particles with arbitrary shapes. It is possible to include

thermal fluctuations in the model by adding a random force on the particle according to Langevin dynamics. However, the reaction on the fluid adjacent to the particle should be modeled properly. In addition, we only consider undeformed particles in this study. When the particle has high aspect ratio, it could bend to change the geometry as well as its velocity. It is interesting to study deformation of a soft particle in an electrokinetic flow and how the geometry of the particle affects the mobility.

## References


1. P. S. Dittrich and A. Manz, “Lab-on-a-chip: microfluidics in drug discovery,” Nat. Rev. Drug Discovery **5**, 210 (2006).

2. K. Ohno, K. Tachikawa, and A. Manz, “Microfluidics: applications for analytical purposes in chemistry and biochemistry,” Electrophoresis **29**, 4443 (2008).

3. M. Napoli, J. Eijkel, and S. Pennathur, “Nanofluidic technology for biomolecule applications: a critical review,” Lab Chip **10**, 957 (2010).

4. R. W. O'Brien, D. W. Cannon, and W. N. Rowlands, “Electroacoustic determination of particle size and zeta potential,” J. Colloid Interface Sci. **173**, 406 (1995).

5. S. Pennathur and J. G. Santiago, “Electrokinetic transport in nanochannels. 1. theory,” Anal. Chem. **77**, 6772 (2005).

6. S. Pennathur and J. G. Santiago, “Electrokinetic transport in nanochannels. 2. experiments,” Anal. Chem. **77**, 6782 (2005).

7. P. Debye and H. Falkenhagen, "Dispersion of the Conductivity and Dielectric Constants of Strong Electrolytes,” Phys. Z. **29** 121 (1928).

8. J. J. Bikerman, “Ionentheory der Elektrosmose der Stromungsstrome und der Oberflaichenleitfaihigkeit,” Z. Phys. Chem. Abt. A: **163**, 378 (1933).

9. J. J. Bikerman, "Electrokinetic equations and surface conductance. A survey of the diffuse double layer theory of colloidal solutions," Trans. Faraday Soc. **36**, 154 (1940).

10. J. J. Bikerman, "Structure and capacity of electrical double layer," Phil. Mag. **33** 384 (1942).

11. B. V. Deryagin and S. S. Dukhin, "Theory of surface conductance," Colloid J. Ussr **31**.277 (1969).

12. J. Lyklema, *Fundamentals of interface and colloid science: soft colloids. Vol. I* (Academic press, 1991).

13. S. S. Dukhin, "Non-equilibrium electric surface phenomena," Adv. Colloid Interface Sci. **44** 1 (1993).

14. J. Lyklema, "On the slip process in electrokinetics," Colloid Surf. A **92** 41 (1994).

15. P. G. Hartley, I. Larson, and P. J. Scales, "Electrokinetic and direct force measurements between silica and mica surfaces in dilute electrolyte solutions," Langmuir **13** 2207 (1997).

16. M. S. Kilic, M. Z. Bazant, and A. Ajdari, "Steric effects in the dynamics of electrolytes at large applied voltages. I. Double-layer charging," Phys. Rev. E **75** 021502 (2007).

17. R. J. Hunter, *Foundations of colloid science* (Oxford University Press, 2001).

18. E. J. Verwey and J. Th. G. Overbeek, *Theory of the stability of lyophobic colloids* (Courier Dover Publications, 1999).

19. J. Lyklema and J. Th. G. Overbeek, "On the interpretation of electrokinetic potentials," J. Colloid Sci. **16** 501 (1961).

20. D. A. Saville, "Electrokinetic effects with small particles." Ann. Rev. Fluid Mech. **9** 321 (1977).

21. M. Z. Bazant, M. S. Kilic, B. D. Storey, and A. Ajdari, "Towards an understanding of induced-charge electrokinetics at large applied voltages in concentrated solutions." Adv. Colloid Interface Sci. **152** 48 (2009).

22. M. von Smoluchowski, "Contribution à la théorie de l'endosmose électrique et de quelques phenomènes," Pisma Mariana Smoluchowskiego **1**, 403 (1924).

23. E. Huckel, "Die kataphorese der kugel," Phys. Z. **25**, 204 (1924).

24. D. Henry, "The cataphoresis of suspended particles. Part I. The equation of cataphoresis," Proc. R. Soc. London. Ser. A **133**, 106 (1931).

25. P. H. Wiersema, A. L. Loeb, and J. Th. G. Overbeek, "Calculation of the electrophoretic mobility of a spherical colloid particle," J. Colloid Interface Sci. **22**, 78 (1966).

26. R. W. O'Brien and L. R. White, "Electrophoretic mobility of a spherical colloidal particle," J. Chem. Soc., Faraday Trans. 2 **74**, 1607 (1978).

27. H. Ohshima, T. W. Healy, and L. R. White, "Approximate analytic expressions for the electrophoretic mobility of spherical colloidal particles and the conductivity of their dilute suspensions," J. Chem. Soc., Faraday Trans. 2 **79,** 1613 (1983).

28. A. S. Khair and T. M. Squires, "The influence of hydrodynamic slip on the electrophoretic mobility of a spherical colloidal particle," Phys. Fluids **21**, 042001 (2009).

29. H. J. Keh and J. L. Anderson, "Boundary effects on electrophoretic motion of colloidal spheres," J. Fluid Mech. **153,** 417 (1985).

30. H. J. Keh and S. B. Chen, "Electrophoresis of a colloidal sphere parallel to a dielectric plane," J. Fluid Mech. **194,** 377 (1988).

31. J. Ennis and J. L. Anderson, "Boundary effects on electrophoretic motion of spherical particles for thick double layers and low zeta potential," J. Colloid Interface Sci. **185** 497 (1997).

32. A. A. Shugai and S. L. Carnie, "Electrophoretic motion of a spherical particle with a thick double layer in bounded flows," J. Colloid Interface Sci. **213** 298 (1999).

33. J. Hsu, M. Ku, and C. Kao, "Electrophoresis of a spherical particle along the axis of a cylindrical pore: effect of electroosmotic flow," J. Colloid Interface Sci. **276**, 248 (2004).

34. J. Hsu and Z. Chen, "Electrophoresis of a sphere along the axis of a cylindrical pore: effects of double-layer polarization and electroosmotic flow," Langmuir **23**, 6198 (2007).

35. Y. Kang and D. Li. "Electrokinetic motion of particles and cells in microchannels." Microfluidic nanofluidic **6**, 431 (2009).

36. K. Ohno, K. Tachikawa, and A. Manz, "Microfluidics: applications for analytical purposes in chemistry and biochemistry," Electrophoresis **29**, 4443 (2008).

37. M. G. L. Van den Heuvel, M. P. De Graaff, S. G. Lemay, and C. Dekker, "Electrophoresis of individual microtubules in microchannels," Proc. Natl. Acad. Sci. **104**, 7770 (2007).

38. T. M. Wynne, A. H. Dixon, and S. Pennathur, "Electrokinetic characterization of individual nanoparticles in nanofluidic channels," Microfluid. Nanofluid. **12**, 411 (2012).

39. M. Napoli, P. Atzberger, and S. Pennathur, "Experimental study of the separation behavior of nanoparticles in micro-and nanochannels," Microfluid. Nanofluid. **10**, 69 (2011).

40. A. J. Russell, J. T. Del Bonis-O'Donnell, T. M. Wynne, M. T. Napoli, and S. Pennathur, "Separation behavior of short single-and double-stranded DNA in 1 micron and 100 nm glass channels," Electrophoresis **35**, 412 (2014).

41. J. Hsu, and C. Kuo, "Electrophoresis of a finite cylinder positioned eccentrically along the axis of a long cylindrical pore," J. Phys. Chem. B, **110**, 17607 (2006).

42. S. M. Davison, and K. V. Sharp “Boundary effects on the electrophoretic motion of cylindrical particles: concentrically and eccentrically-positioned particles in a capillary,” J. Colloid Interface Sci. **303**, 288 (2006).

43. D. L. House, and H. Luo, “Electrophoretic mobility of a colloidal cylinder between two parallel walls,” Eng. Anal. Boundary Elem. **34** 471 (2010).

44. H. Liu, H. H. Bau, and H. H. Hu, “Electrophoresis of Concentrically and Eccentrically Positioned Cylindrical Particles in a Long Tube,” Langmuir **20** 2628 (2004).

45. Y. Liu, S. Pennathur, and C. D. Meinhart. "Electrophoretic mobility of a spherical nanoparticle in a nanochannel," Phys. Fluids **26**, 112002 (2014).

46. S. M. Davison, and K. V. Sharp, " Transient electrophoretic motion of cylindrical particles in capillaries,” Nanosci Microsci Therm **11** 71 (2007).

47. Y. Ai, and S. Qian, “Direct numerical simulation of electrokinetic translocation of a cylindrical particle through a nanopore using a Poisson–Boltzmann approach,” Electrophoresis **32** 996 (2011).

48. J. Hsu, L. Yeh, and M. Ku, “Evaluation of the electric force in electrophoresis,” J. Colloid Interface Sci. **305**, 324 (2007).

49. E. L. Cussler, *Diffusion: mass transfer in fluid systems* (Cambridge university press, 2009).

50. D. Gillespie and S. Pennathur, “Separation of ions in nanofluidic channels with combined pressure-driven and electro-osmotic flow,” Anal. Chem. **85**, 2991 (2013).

51. Śmiałek MA, Jones NC, Hoffmann SV, Mason NJ (2013) Measuring the density of DNA films using ultraviolet-visible interferometry. Phys Rev E 87:060701

52. T. M. Squires, and M. Z. Bazant, "Induced-charge electro-osmosis," J. Fluid Mech. **509** 217 (2004).

53. C. W. Hirt, A. A. Amsden, and J. L. Cook, “An arbitrary Lagrangian-Eulerian computing method for all flow speeds,” J. of Comp. Phys., **14** 227 (1974).

54. J. Donea, A. Huerta, J. P. Ponthot, and A. Rodríguez-Ferran, “Arbitrary lagrangian–eulerian methods,” Encyclopedia of computational mechanics (2004).

55. H. Morgan, and N. G. Green, *AC electrokinetics: colloids and nanoparticles* (Research studies press, 2003).

56. I. Semenov, S. Raafatnia, M. Sega, V. Lobaskin, C. Holm, and F. Kremer, “Electrophoretic mobility and charge inversion of a colloidal particle studied by single-colloid electrophoresis and molecular dynamics simulations,” Phys. Rev. E, **87** 022302 (2013).